Multi-objective optimisation and verification of creep resistant Ni-base superalloy for electron-beam powder-bed-fusion

Shen Tao[a,b,1], Yansong Li[a,b,1], Hui Peng[a,b,*], Hongbo Guo[b], Bo Chen[c*]

[a]*Research Institute for Frontier Science, Beihang University, Beijing 100191, China*

[b]*School of Materials Science and Engineering, Beihang University, Beijing 100191, China*

[c]*School of Engineering, University of Southampton, Southampton, SO17 1BJ, UK*

*Corresponding authors. E-mail address: *b.chen@soton.ac.uk, *penghui@buaa.edu.cn

[1]These authors contributed equally to this work.

Abstract

This paper reports the use of integrated computational alloy design, coupled with a rapid printability screening method, to downselect from a total of 70000 dataset in design space to five candidates in the first step, and then from five to one in the second step. The new Ni-base superalloy with compositions of Ni-5.03Al-2.69Co-5.63Cr-0.04Hf-1.91Mo-2.36Re-3.32Ta-0.57Ti-8.46W-0.05C-0.019B exhibits an optimal balance of density (8.82 g/cm^2), printability (freezing range of 107 °C), thermal stability (γ′-volume fraction of 50.7% at 980 °C and low $\overline{M_d}$ value) and creep (rupture time of 612 h at 980 °C/120 MPa). The micro-hardness varies mildly from 417.2±18.5 to 434.7±14.6 Hv, suggesting a good phase stability. This is substantiated by microstructure observations, which revealed the absence of a topologically close packed phase. Machine-learning tools of the artificial neural network (ANN), random forest and support vector regression, respectively, were used to predict creep rupture time. The ANN algorithm achieves the highest accuracy in predicting creep life. By recognising the "black box" nature of the ANN, interpretability analysis was conducted using the local interpretable model-agnostic method. The analysis supports that the ANN model truly learned meaningful functional relationships, and thus is judged as reliable. Feature correlation evaluation outcome emphasises the importance of incorporating microstructure-related input feature.

Keywords: Alloy design; Ni-base superalloys; Additive manufacturing; Machine learning; Creep

1. Introduction

Designing high-temperature structural materials such as Ni-base superalloys that involve more than 10 alloy elements require significant time and capital investment. This is because correlation between the composition and material property represents a high-dimensional problem and shows complex data relationships [1]. The overall target of alloy design is to find the optimal compositional combination that maximises the performance index. A cost-effective workflow, encompassing compositional design, processing and verification, is demonstrated in the present work through developing a non-weldable Ni-base superalloy with the attributes of low density, good thermal stability, crack-free 3D printing and creep life. Fig. 1 depicts how the integrated computational tool system, coupled with carefully selected rapid printability screening experimental methods, was implemented to achieve our goal. The research hypothesis is by connecting the dots, the time and cost associated with the design and qualification of a new Ni-base superalloy tailored for additive manufacturing (AM) can be vastly reduced. This work is motivated by two previous AM studies, and the identified gaps are highlighted next.

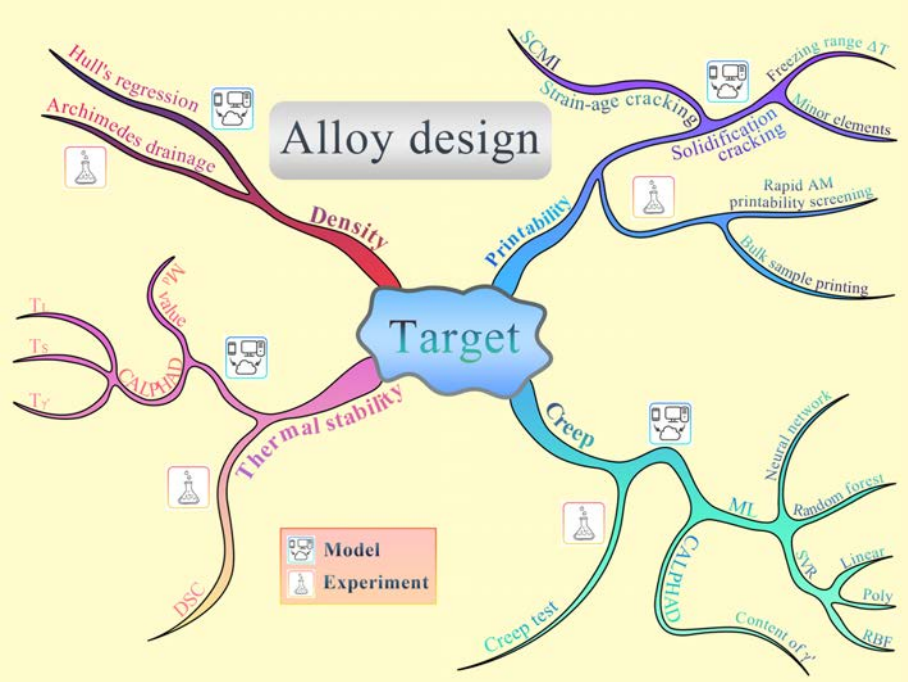

Fig. 1: Schematic summary of the integrated tool system, involving both the digital tools and rapid AM printability screening experiments, to achieve the target of alloy design.

Pollock et al. [2] developed a new CoNi-base superalloy SB-CoNi-10, printable for both the electron-beam and laser-beam powder-bed-fusion (EB-PBF and L-PBF) AM processes, by using computational and rapid AM printability screening alloy design tools (e.g., first-principles calculations, CALPHAD approach based on thermodynamic calculations, combinatorial alloy processing and characterisation techniques). Their alloy design criteria involved good high-temperature strength and oxidation resistance in addition to the printability. The resulting material was proven as AM defect-resistant, exhibiting excellent tensile properties at room temperature. Reed et al. [3] designed two new crack-free superalloys ABD-850AM and ABD-900AM (belonging to the weldable group) tailored for the L-PBF using CALPHAD approach. The present work, by contrast, studies the machine learning (ML) aided design of non-weldable Ni-base superalloy, tailored for the EB-PBF. Moreover, our alloy design toolkit was coupled with the new rapid printability screening method. This helps to tackle one of the challenges in the AM domain, i.e., fabrication of expensive powders with significant quantities [2].

ML has become the mainstream for developing new material systems thanks to its higher efficiency, continually improved accuracy, and lower cost [4,5]. It has achieved successes for optimising stainless steels [6–10], permanent magnets [11], shape memory alloys [12], metallic glasses [13], composites [14], and Ni-base superalloys [15–18]. Especially, ML is proven as an effective tool for the alloy design in terms of linking the alloy composition to material properties. Case studies cover both the physical and mechanical properties, such as electrical conductivity [19], transformation temperature [12], fatigue [8], tensile [6,19,20] and creep [9,15–18], to name a few. For example, Conduit et al. [15] applied a set of artificial neural network (ANN) algorithms to design a new Ni-base superalloy exceeding the target criteria of fatigue life, tensile property, and creep life. However, no experimental verification was conducted. Another example is the work of Montakhab and Balikci [18], where the ANN method was coupled with physics-based calculations to predict the creep life of Ni-base superalloy. But they were not able to prepare alloy compositions with better creep life as predicted by the ANN method. By combining the rapid AM printability screening design strategy with unsupervised ML method in [21], the prediction of creep rates and structural stability of Ni-base superalloys became more efficiently through the massive calculations of the multi-element diffusion coefficients. Generally speaking, all studies were exclusively focused on cast and wrought Ni-base superalloys. In this

context, the present work represents the first report of employing the ML-aided alloy design tool for the development of AM Ni-base superalloy, together with the experimental verification.

AM printability of the non-weldable Ni-base superalloy has been a hot topic over the last decade, with published work of e.g., [22–24]. In brief, the crack susceptibility can be minimised by first, lowering the sum of Al, Ti, Ta and Nb concentrations (e.g., [3]) and second, lowering the $\left|dT/d(f_S^{1/2})\right|$ near $(f_S^{1/2})$=1 (e.g., [25]) or narrowing the freezing temperature range (e.g., [2] The former is associated with the strain-age cracking whilst the latter with solidification cracking mechanism. Thermal stability of Ni-base superalloy appears to be another concern, especially for the EB-PBF where the high build temperature was found to promote the formation of topologically close packed (TCP) phase [26] at the lower build height region. Latest work by Liu et al. [27] demonstrated that adding minor Sc to Ni-base superalloys can greatly improve the AM printability and material properties.

Here, we design a new AM Ni-base superalloy that simultaneously fulfils four criteria: printability, creep, thermal stability and density. Our significant contribution lies in the integration of alloy design and rapid AM printability screening characterisations to achieve a cost-effective processing. In the first part of the paper, the computational alloy design methodology and digital tools involved are described, followed by explaining how the rapid material screening was achieved to downselect the top five alloy types. The next major part of the paper is devoted to describing the rapid AM printability screening verification methodology, followed by evaluating the robustness of the chosen digital tools via direct experimental data comparison. Given that the newly designed non-weldable but AM printable Ni-base superalloy has an experimental creep life of 612 h at 980 °C/120 MPa as compared to that of 603 h from the ANN prediction, the discussion part seeks to interpret the prediction results and extract important knowledge from the ML model.

2. Integrated computational alloy design

2.1 Methodology

Table 1 lists the digital approaches used to predict properties together with the target specifications. Physical approaches were used to calculate the strain-age cracking

merit index (SCMI), d-orbital energy level ($\overline{M_d}$) and density (ρ). CALPHAD approach was used to derive the liquidus and solidus temperatures (T_L and T_S), γ′ solidus temperature ($T_{\gamma'}$), freezing temperature range ($\Delta T = T_L - T_S$), and the content of γ′ at 980 ºC. Machine-learning tools of the ANN, random forest (RF) and support vector regression (SVR), respectively, were used to predict the creep rupture time at 980 ºC/120 MPa.

Table 1: Approach used to predict properties and the target specification

Property	Approach	Target
SCMI	Physical	SCMI>4 wt.%
M_d value	Physical	$\overline{M_d}$<0.98 eV
Density	Physical	ρ<9.1 g/cm^3
Liquidus temperature	CALPHAD	T_L>1300 ºC
Solidus temperature	CALPHAD	T_S>1250 ºC
Freezing temperature range	CALPHAD	ΔT<200 ºC
Content of γ′ at 980 ºC	CALPHAD	γ′ content>50%
γ′ solidus temperature	CALPHAD	$T_{\gamma'}$>1100 ºC
Rupture time at 980 ºC /120 MPa	Machine learning (ML)	t>500 h

2.2 Creep

The primary distinction among evolving generations of single-crystal Ni-base superalloys lies in their Re concentration, with the second generation being the most prevalent in the market. For a typical first-generation single-crystal Ni-base superalloy, it does not contain Re element; by comparison, a second-generation single-crystal Ni-base superalloy contains about 3 wt.% Re, whilst a third-generation superalloy contains between 5 and 6 wt.%. It is also worthwhile noting that the addition of Ru has become a mainstream when designing the latest ‘fourth-generation’ single-crystal superalloys [28]. Typical elements used in the second-generation single-crystal Ni-base superalloys are Ni, Al, Co, Cr, Hf, Mo, Re, Ta, Ti and W, without taking into account the trace elements. 70000 groups of data, which were randomly generated within the composition range as indicated in Table 2, were used as the test data. 1013 groups of data, spanning from the low to high creep temperatures and stress levels for a wide range of alloy types, were sourced from the published papers (e.g., [29–34]), books (e.g., [28]), online database (e.g., [35,36]) and our unpublished work. They were used as the known data for the ANN prediction of creep life, by serving as the training and

validation data. Five ML algorithms were compared, including ANN, RF, and three SVR sub-categories.

Table 2: Composition ranges used to generate the alloy design space

Elements	Ni	Al	Co	Cr	Hf	Mo	Re	Ta	Ti	W
Range (wt.%)	Bal.	1-6	2-10	0-7	0-0.5	0-4	0-5	2-10	0-1	2-10

The ANN algorithm was chosen as it can map the relationship between different compositions and material property by fast learning of a large dataset. Additionally, it can be combined with optimisation algorithms to analyse the weights and biases, facilitating iterative optimisation to identify the optimal alloy composition. The RF algorithm is another commonly used ML model based on decision tree [37]. The SVR algorithm is developed from support vector machine [38], and it requires appropriate parameter selection (e.g., kernel function, penalty factor C, gamma and epsilon), and data pre-processing to fully exploit its advantages. Three types of kernel functions were considered: linear kernel (SVR.lin), polynomial kernel (SVR.poly), and radial basis function kernel (SVR.rbf). All of the ML algorithms were realised using sklearn in Python with the same dataset. Due to sufficient and evenly distributed data, we directly adjust the hyperparameters of each model by partitioning the data. Different ML models have their pros and cons. For example, compared to the ANN algorithm, RF is more user-friendly, requiring fewer hyperparameter adjustments and enabling faster training and optimisation; and SVR can efficiently handle high-dimensional data while keeping the data interpretation straightforward. However, the prediction accuracy determines their fit-for-purpose.

The evaluation of each algorithm performance was based on the root mean squared error (RMSE), mean absolute error (MAE) and coefficient of determination (R^2):

$$\mathrm{RMSE} = \sqrt{\frac{1}{N}\sum_{i=0}^{N-1}(y_i - \hat{y}_i)^2} \quad (1)$$

$$\mathrm{MAE} = \frac{1}{N}\sum_{i=0}^{N-1}|y_i - \hat{y}_i| \quad (2)$$

$$R^2 = 1 - \frac{\sum_{i=0}^{N-1}(y_i - \hat{y}_i)^2}{\sum_{i=0}^{N-1}(y_i - \bar{y})^2} \quad (3)$$

where N is the data number, y_i is the experimental value, $\hat{y}_i$ is the predicted value, and $\bar{y}$ is the average value of the creep life. The prediction is judged as more accurate when the values of RMSE and MSE are smaller and the R^2 value is closer to 1.

The ANN algorithm deserves a further description for two reasons: first, this ML tool performs the best for predicting the creep life when compared to the other four; second, both the number of hidden nodes and epoch selections are known to greatly influence the prediction results [18]. In this work, a 13-11-1 neural network structure was chosen, with 13, 11 and 1 representing the input layer, hidden nodes, and the output layer (i.e., creep rupture time), respectively. The 13 input layer data included 10 element types (Table 2), the γ′ content, creep temperature and stress. 11 hidden nodes were chosen as this number led to the lowest value of RMSE, Fig. 2a. Furthermore, the optimal model complexity was evaluated by finding the best bias-variance trade-off in terms of the optimal epoch, namely, the number of times that the algorithm went through the entire training dataset. As shown in Fig. 2b, despite the monotonic decline of the training loss with the number of epochs, the validation loss reached its minimum at 400 epochs, indicating the presence of data overfitting. Thus 400 was chosen for the present ANN model.

Adaptive moment estimation (so-called Adam) was used for training as opposed to the traditional stochastic gradient descent [15]. This optimisation algorithm can design independent adaptive learning rates for different parameters by computing first-order and second-order moment estimates of the gradients [39]. Training cycle was terminated when generalisation stopped improving. Rectified linear unit (ReLU) activation function acting on the output neurons was used to transform input into output signals. When compared to the Sigmoid and Tanh functions used in previous work [15,18], the ReLU function has its advantages of sparse activation, mitigating gradient vanishing, and linear separability.

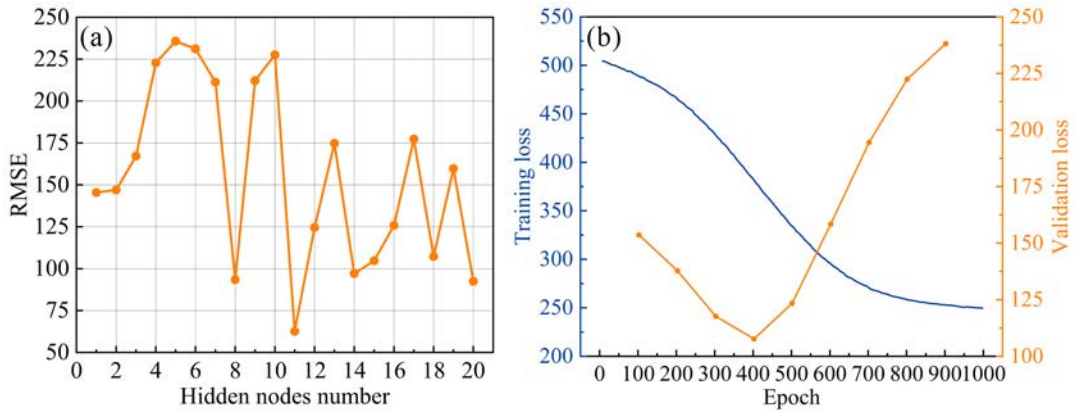

Fig. 2: (a) Influence of the number of hidden nodes on RMSE; (b) evolution of the training loss and validation loss as a function of epoch.

2.3 Printability and thermal stability

Thermodynamic calculations of the CALPHAD approach were performed with the TCNI10 database using Thermo-Calc software. Given the large amount of data in the design space, TCPython, a software development kit attached to the Thermo-Calc, was used to greatly accelerate the calculation efficiency. The Scheil-Gulliver model was used to calculate the non-equilibrium solidification behaviour. In general, the higher the calculated phase transformation temperatures, the better the material performance at high temperature. Thus, the following target criteria were set: T_L>1300 ºC, T_S>1250 ºC, and $T_{\gamma'}$>1100 ºC (Table 1). Moreover, the magnitude of freezing temperature range needs to be smaller than 200 ºC (ΔT<200 ºC in Table 1) so that the Ni-base superalloy is less prone to the solidification cracking during the AM process [2].

In general, adding more solid solution strengthening elements such as Mo, Co, W can greatly improve the strength [40], while low Si and C contents help in avoiding crack formation [41]. Besides, the addition of C and B can also improve the creep life [42]. However, their contents should be strictly controlled [43,44]. Després et al. [45] found that the Ni-base superalloy with B+C addition exhibited a better creep resistance than the C addition alone. When the C content reduced to 0.05 wt.%, adding B stabilised grain boundaries [46,47]. But excessive B addition resulted in the formation of solidification cracks [48].

Here, an empirical method was adopted to set the limit, as opposed to using the ML method as their minor concentration is deemed to propagate a large error. The relationship between the Cr, Mo and B contents (in at.%) was defined as:

$$k = \frac{0.416}{[\mathrm{Cr+Mo}]^5[\mathrm{B}]^3} \quad (4)$$

where k is the solubility product. According to [49], the critical value of k=0.012 was used to calculate the optimum B concentration. The C concentration was set as 0.05 wt.% in this work.

Among the considered elements in Table 2, according to Thompson et al. [50] and Henderson et al. [51], Al, Ti and Ta can promote the γ′ formation and thereby compromises the material's local ductility, leading to strain-age cracking. Their combined effect can be defined through the SCMI factor:

$$\mathrm{SCMI} = W_{Al}+0.5W_{Ti}+0.15W_{Ta} \text{ (all in wt.\%)} \quad (5)$$

The so-called weldability diagram, therefore, can be drawn by using the Al concentration as abscissa whilst the combined concentration of Ti and Ta (i.e., $0.5W_{Ti}+0.15W_{Ta}$) as ordinate. Using the SCMI as the boundary line, when the SCMI value is higher than 4 wt.%, the Ni-base superalloy is considered non-weldable. Obviously, the higher the SCMI factor, the higher the γ′ fraction. This represents a trade-off between the improved creep performance and worse AM printability. For this reason, the design criterion was set as reasonably close to the boundary line but greater than 4 wt.% for the newly designed non-weldable Ni-base superalloy.

During the casting or welding process, certain alloys are prone to cracking due to the solidification shrinkage caused by the higher density of the solid than the liquid. Therefore, during the final solidification process, cracks may occur along grain boundaries, according to Kou [25]. In that work, a crack susceptibility index, defined as $\left|dT/d(f_S^{1/2})\right|$ near $(f_S^{1/2})$=1, was proposed to evaluate the solidification crack susceptibility. Given the absolute value of slope of the curve varies significantly near $(f_S^{1/2})$=1, an average steepness $\left|\Delta T'/\Delta(f_S^{1/2})\right|$ was used as an approximation. Note that the higher the crack susceptibility index, the higher susceptibility of the alloy to solidification cracking. In the present work, this index has been used to evaluate the susceptibility of designed superalloys to solidification cracking.

Most of the main alloy elements in Ni-base superalloys are transition elements with unpaired d-electrons (e.g., Co, Cr, Mo, Re, Ta and W with their anticipated concentration ranges listed in Table 2). Covalent bond strength between the d-electrons, responsible for the high cohesive energy of transition metals, can be informed by using two physical parameters: d-orbital energy level (M_d) and the bond order [52–54]. The list of M_d values for all the elements listed in Table 2 can be found in [53]. For example, the higher M_d values were found for Hf (3.020 eV) and Ta (2.224 eV) than the others (e.g., Co of 0.777 and Re of 1.267 eV). This means that for the same amount of alloy addition, elements with higher M_d are expected to have an adverse effect on the thermal stability. In practice, the average M_d value (symbolised with $\overline{M_d}$) of a particular superalloy type was derived using:

$$\overline{M_d} = \sum X_i (M_d)_i \quad (6)$$

where X_i is the atomic fraction of element i, and $(M_d)_i$ is the M_d value for that particular element. The higher $\overline{M_d}$ value indicates the greater tendency of the TCP-phase formation [55], and hence the target criterion was set as $\overline{M_d}$<0.98 eV (Table 1).

2.4 Density

The density of pure Ni at room temperature is 8.9 g/cm^3, but alloying changes its value, with most of the 5d transition elements significantly increasing the alloy density, such as the refractory elements of Re, W and Ta. Fig. 3 shows the density values of Al and transition elements from 3d to 5d series, with a total of 10 chosen elements marked to illustrate such effect. The superalloy density can be estimated with the density of pure elements by using the Hull's regression equation (all in wt.%), under the premise of no element mixing or interaction [56]:

$$\boldsymbol{\rho}=[\boldsymbol{\omega}+0.1437-0.00137W_{Cr}-0.00139W_{Ni}-0.00142W_{Co}-0.00125W_{W}-0.00113W_{Ta}+0.00040W_{Ti}-0.00113W_{Hf}+0.0000187(W_{Mo})^2-0.0000506(W_{Co})(W_{Ti})]\times 27.68\ (g/cm^3),\ \text{with}\ \boldsymbol{\omega}=[100/[\sum_{i=1}^{n}\frac{W_i}{D_i}] \quad (7)$$

where W_i stands for the wt.% of element i, and D_i is the density of pure element i. Here the upper limit of density was set as ρ<9.1 g/cm^3.

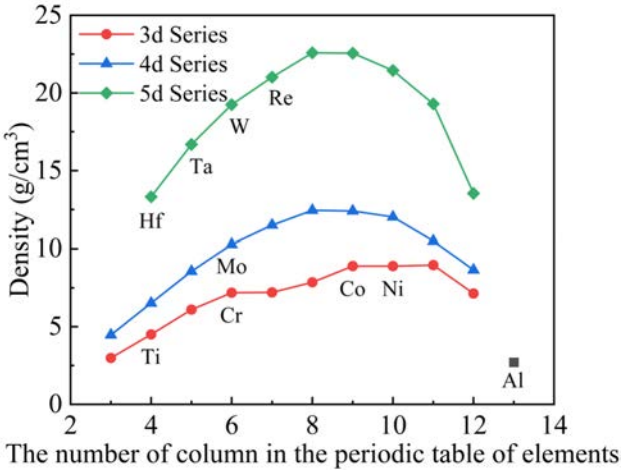

Fig. 3: Density of transition elements in 3d, 4d and 5d series as well as Al element at room temperature. Note that density of 10 elements selected for alloy design were marked.

3. Alloy design results

Fig. 4a compares five ML algorithms used for the creep life prediction, and their performance was assessed based on the values of the RMSE and MAE (Eqs. 1 and 2). Both the ANN and SVR.rbf models have the lowest values, meaning that they can

predict the creep life with good accuracy, followed by the RF algorithm. Fig. 4b-4f present the one-to-one comparison between experimentally obtained (abscissa) and modelling predicted (ordinate) creep life, for the ANN, RF, and three SVR models, respectively. Blue points are from the validation data while red line is the regression line. It can be seen that the R^2 values of the ANN and SVR.rbf models are above 0.98, indicating a good prediction. By comparison, the data distribution of SVR.lin and SVR.poly are asymmetric with reference to the red line, suggesting that the low R^2 value for these two models was caused by the extreme "bad points". In terms of the RF model, its R^2 value is lower than the ANN and SVR.rbf, but the prediction was not misled heavily by the extreme values, Fig. 4c. The ANN predicted creep life will hereafter be chosen, because it has received a steady improvement not only on its accuracy but also on the intepretability; with the latter leading to a gradual uncovering of how each input feature contributes to the overall model performance.

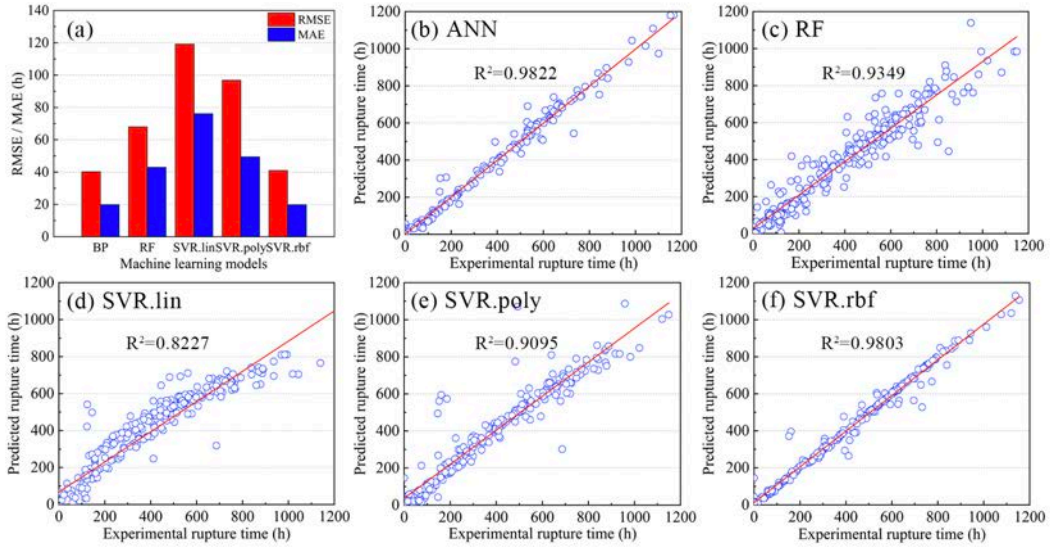

Fig. 4: (a) Comparison of the algorithm performance based on RMSE/MAE values for the five machine learning methods; (b) to (f) one-to-one comparison of the model predicted against experimental observed creep rupture time, for the ANN, RF, SVR.lin, SVR.poly, and SVR.rbf, respectively, with the value of R^2 marked in each figure.

Based on the target criteria, the top 5 alloy compositions were identified, and they are summarised in Table 3. To better visualise the relationship between compositions and properties, the alloy design space used for screening out the new superalloy grades are shown in Fig. 5. For comparison purposes, data points representing the current second-generation Ni-base single crystal superalloys are marked with green colour, and the colour partitioned regions reflect the set criterion.

Table 3: Alloy compositions for the top 5 Ni-base superalloys which meet all four design criteria (all in wt.%)

Alloy ID	Ni	Al	Co	Cr	Hf	Mo	Re	Ta	Ti	W	C	B
1	Bal.	5.14	3.00	4.19	0.22	2.29	2.77	3.29	0.16	8.65	0.05	0.026
2	Bal.	5.08	3.97	4.35	0.2	2.43	2.74	2.98	0.21	8.91	0.05	0.024
3	Bal.	5.04	2.36	6.45	0.19	2.72	1.59	3.29	0.39	8.78	0.05	0.014
4	Bal.	5.03	2.69	5.63	0.04	1.91	2.36	3.32	0.57	8.46	0.05	0.019
5	Bal.	4.91	2.44	5.58	0.31	1.39	3.35	2.74	0.39	9.07	0.05	0.020
René N5	Bal.	6.0	8.0	7.1	0.15	2.0	3.0	7.0	0	5.0	0.05	0.004

The newly designed superalloys are closer to the dividing line between the weldable and non-weldable types, when compared to the existing ones, Fig. 5a. This means that they are less prone to the strain-age cracking. On the flip side, the five alloys tailored for AM belong to the non-weldable group, which represents a fundamental difference to the ABD-850 and ABD-900 alloys as reported previously [3]. Fig. 5b presents the γ′-volume fraction at 980 ºC versus the SCMI factor which essentially combines the ordinate and abscissa values as presented in Fig. 5a. It can be seen that the newly designed five superalloys have a reasonably high γ′-volume fraction (above 50%) whilst keeping a lower SCMI value.

Furthermore, the freezing temperature range of the top five superalloys is less than 200 ºC, Fig. 5c, suggesting a lower tendency to solidification cracking. Interesting to note, all the existing Ni-base superalloys, except for the MC2 type, are prone to solidification cracking, and thus they are not ideal for the AM process. Based on the Thermo-Calc calculations, crack susceptibility index $\left|dT/d(f_S^{1/2})\right|$ near $(f_S^{1/2})$=1 has been also used to evaluate the solidification cracking susceptibility of five designed alloys. The terminal solidification path of alloy 1 to 5 is illustrated in Fig. 5e, with the dark-grey area indicating the region of $f_S^{1/2}$=0.933 (f_S=0.87) and 0.970 (f_S=0.87), according to [25,57–59]. The temperature changes $\Delta T'$ in the selected f_S range of alloy 1 to 5 are 39, 40, 42, 36, and 43 °C, respectively, as shown in Fig. 5f. The corresponding crack susceptibility index was calculated as 1054, 1081, 1135, 973 and 1162 for alloy 1 to 5. With the same f_S range, alloy 4 apparently has the lowest $\Delta T'$ and crack susceptibility index among five designed alloy, whilst alloy 5 has the highest value.

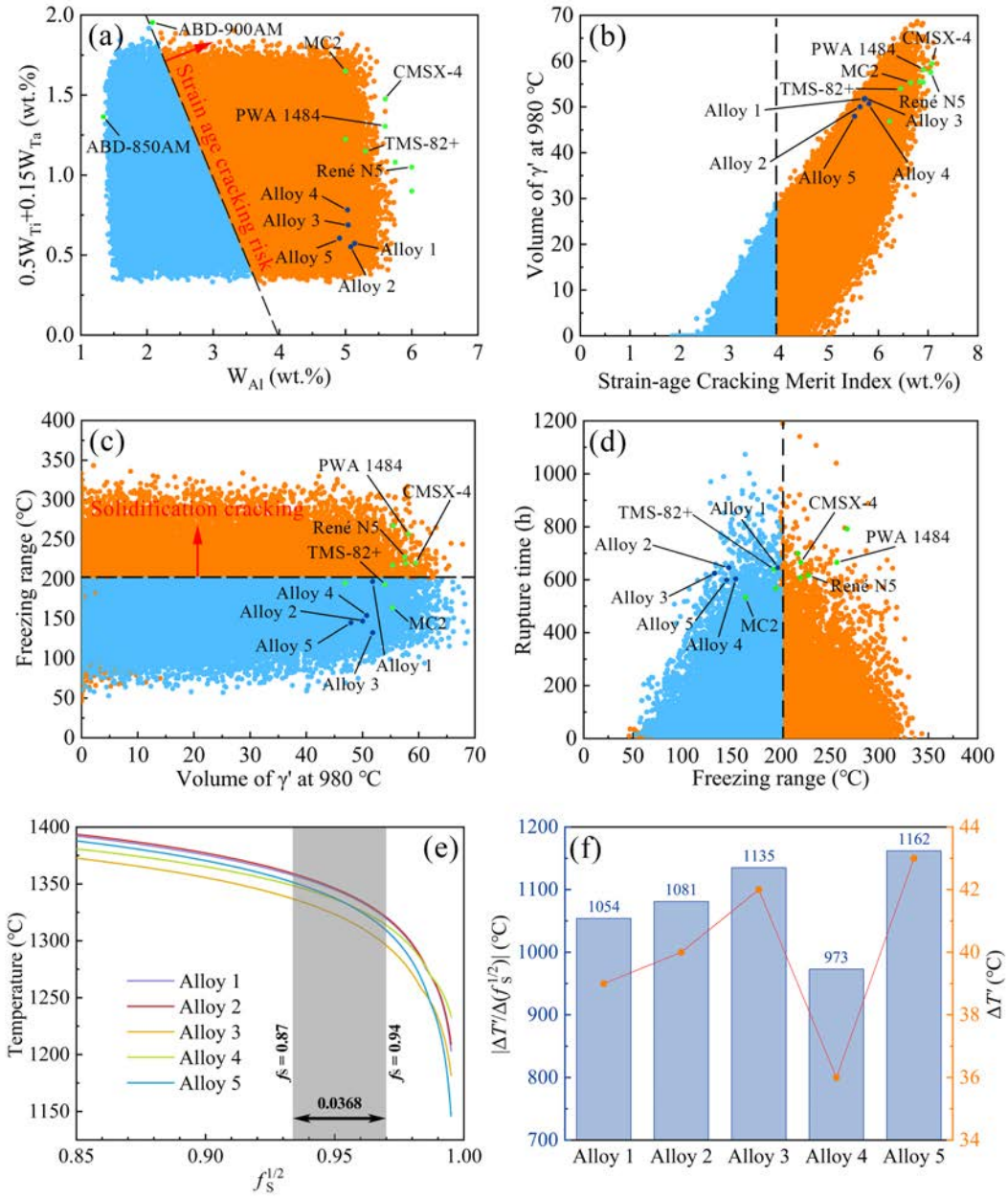

Fig. 5: Plots of 70000 data used for the computational alloy design, with both the newly designed alloy types (named as alloy 1 to 5) and the widely used second-generation Ni-base single crystal superalloys marked in the design space: (a) SCMI plot to indicate strain-age cracking susceptibility; (b) γ′-volume fraction; (c) freezing temperature range; (d) creep rupture time; (e) and (f) solidification cracking susceptibility of the newly designed alloy 1 to 5, plotted using the criterion proposed by Kou [25]. Note: the two newly designed AM compatible Ni-base superalloys ABD series [3] are also indicated in (a) to visualise their weldable nature.

Fig. 5d presents the ANN model predicted creep life, and all of the newly designed superalloys exhibit a good balance of creep performance and AM printability. As informed by the ML model, the trade-off between the two is overcome by increasing the overall concentration of solid solution strengthening elements (e.g., Mo and W).

For example, René N5 is a second-generation Ni-base single crystal superalloy, and it contains a higher concentration of Al, Ti and Ta, but the combined concentration of Mo and W is lower, when compared to alloys 1 to 5 (Table 3).

Thermal stability and density are the other two alloy selection criteria (Fig. 1). The former was addressed using the $\overline{M_d}$ method. The top five alloy types have the $\overline{M_d}$ value of 0.970, 0.970, 0.979, 0.970, 0.970 eV, respectively, which are lower than the existing Ni-base superalloys, e.g., René N5 of 0.989 eV and CMSX-4 of 0.984 eV. Thus, they are expected to have a good thermal stability, which is beneficial for a reduced tendency to form TCP phase and thereby showing a good compatibility with the EB-PBF AM process [26]. The violin-histogram plot in Fig. 6a, based on the calculated density, exhibits a normal distribution feature, indicating a well-representing alloy design space.

Fig. 6b compares the model calculated with experimentally measured density for a range of existing Ni-base superalloys. The linear least-squares fitting returns to a value of k=1.06, indicating that the calculated density would be higher than the measured one, with the relative error estimated as 1-3%. The reason for such discrepancy is due to atom mixing which is not considered by the Hull's regression. To this end, the density criterion was set as $\rho < 9.1$ g/cm^3 from the modelling perspective, however, the expected density from the measurement would likely fall into the density range of 8.64-8.95 g/cm^3 based on the one-to-one comparison of the existing second-generation single-crystal Ni-base superalloys, as indicated in Fig. 6b.

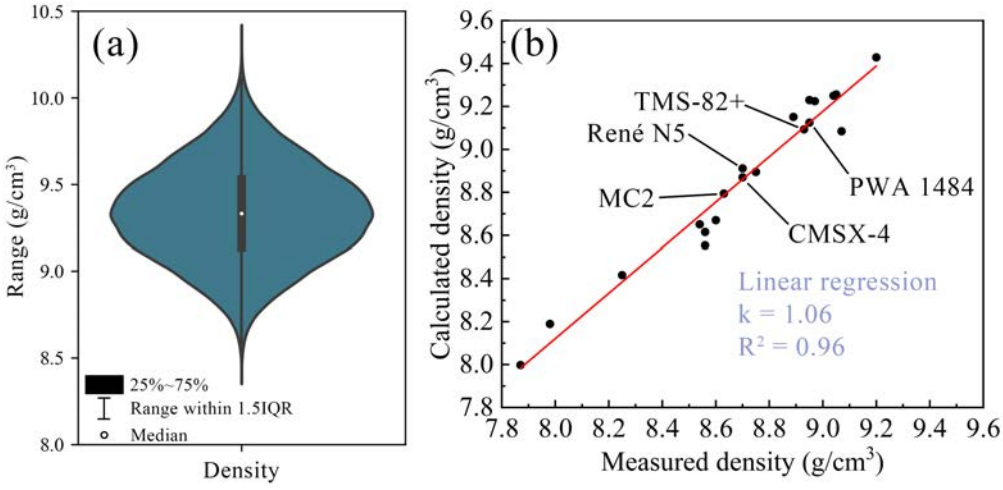

Fig. 6: (a) Violin-histogram of the calculated density for the considered 70000 data; (b) one-to-one comparison of the measured and calculated density for the existing Ni-base superalloy types.

4. Experimental verification

4.1 Rapid AM printability screening and crack susceptibility evaluation

First, cast alloy sample coupons with dimensions of 50×25×5 mm^3 were made using the five different alloy compositions as shown in Table 3. Casting was performed in a vacuum arc melting furnace with 99.99% high purity argon filled. This step involved ingot overturning smelting of 7 times (5 mins per time), with the use of electromagnetic stirring during the smelting, and finally cooling to room temperature. Second, the as-cast sample coupon was cut into a cuboid with dimensions of 10 mm long and 5 mm wide. Third, the cuboidal specimen was placed inside a recession cut into a stainless-steel starting plate with dimensions of 105×105×10 mm^3. Fig. 7a illustrates how the cuboidal specimens were positioned in the starting plate.

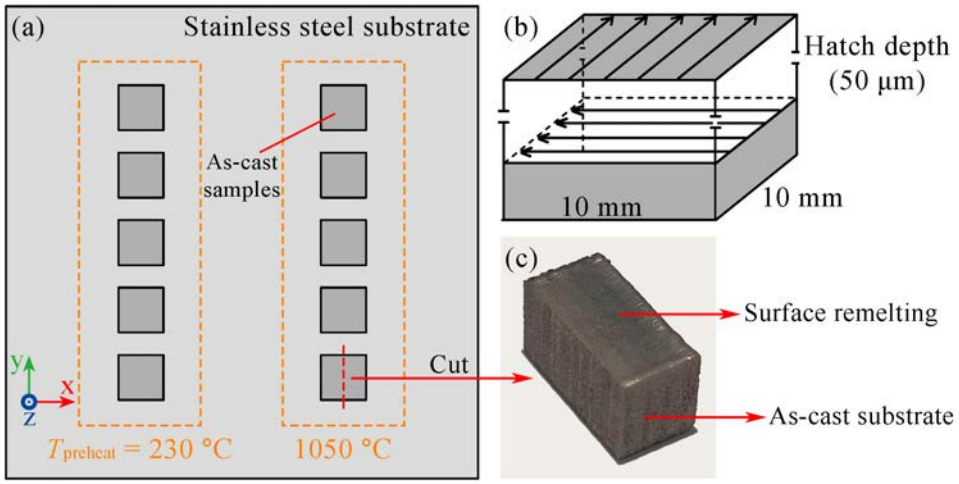

Fig. 7: (a) A schematic showing the sample layout for conducting the EB-PBF surface remelting; (b) scan strategy; (c) a photograph showing a representative sample in the surface remelted condition. Note that each sample was cut from the middle position to examine the cracking behaviour.

Prior to the surface remelting, preheat step was applied. As shown in Fig. 7a, two different preheat temperatures (i.e., $T_{preheat}$=230 °C and 1050 °C) were considered to examine the cracking susceptibility. We heated the substrate to 1050 °C for the right five alloys, cooled to room temperature, and then preheated to 230 °C for the left five ones. For the surface remelting itself, beam power P of 600 W, scan speed v of 2000 mm/s, line offset L_{off} of 0.1 mm, and line order of 99 were chosen, resulting in the area energy value of 3 J/mm^2. Note that the same process parameter set was used later on to

fabricate the bulk sample. The preheat, surface remelt and bulk sample fabrication were all conducted using the EB-PBF machine (Arcam A2XX). The machine was operated in manual mode, and each cuboidal sample was subjected to remelting twice, as shown in Fig. 7b. Hatch depth was set as 50 μm and the hatch direction was rotated by 90° between layers. A typical sample in the surface remelted condition is shown in Fig. 7c, together with the indication of the vertical cut position. The cut was made perpendicular to the beam scan direction of the second scan used for the surface remelting.

Crack examination was performed on the horizontal cross-section with the help of scanning electron microscopy (SEM, Zeiss Supra-55), and then on the vertical cross-section with the aid of optical microscopy (Zeiss AxioCam MRc 5). For the SEM observation of Fig. 8, sample's surface condition was in the as-cut state, whilst mechanically polished sample down to 0.5 μm diamond paste was used for the optical microscopy of Fig. 9.

The left column of Fig. 8a to 8e are the surface remelted samples with the preheat temperature of 230 °C, whilst the right column of Fig. 8f to 8j are those with the preheat temperature of 1050 °C. As revealed by the SEM examination, the cracks would always form regardless of the alloy compositions under the preheat temperature of 230 °C. By contrast, the number of cracks vastly reduced under the preheat condition of 1050 °C. Especially, alloys 1 to 4 showed virtually no crack, Fig. 8f to 8i. However, alloy 5 still exhibited cracks despite the high preheat temperature, Fig. 8j. To a certain extent, this rapid screening test substantiates that the newly designed Ni-base superalloys are well suited for the EB-PBF method as opposed to the L-PBF (operating at low build temperature). Alloys 1 to 5 (1050 °C preheat temperature) were examined further on a large cross-section prepared vertically, as shown in Fig. 9. Alloy 4 was ranked the best (i.e., immune to cracking), followed by alloys 3, 1, 2 and 5, in order of low to high crack susceptibility. Henceforth, alloy 4 with the composition of Ni-5.03Al-2.69Co-5.63Cr-0.04Hf-1.91Mo-2.36Re-3.32Ta-0.57Ti-8.46W-0.05C-0.019B (Table 3) is verified as a Ni-base superalloy with good EB-PBF compatibility with the use of cost-effective surface remelting (i.e., without producing mass powders).

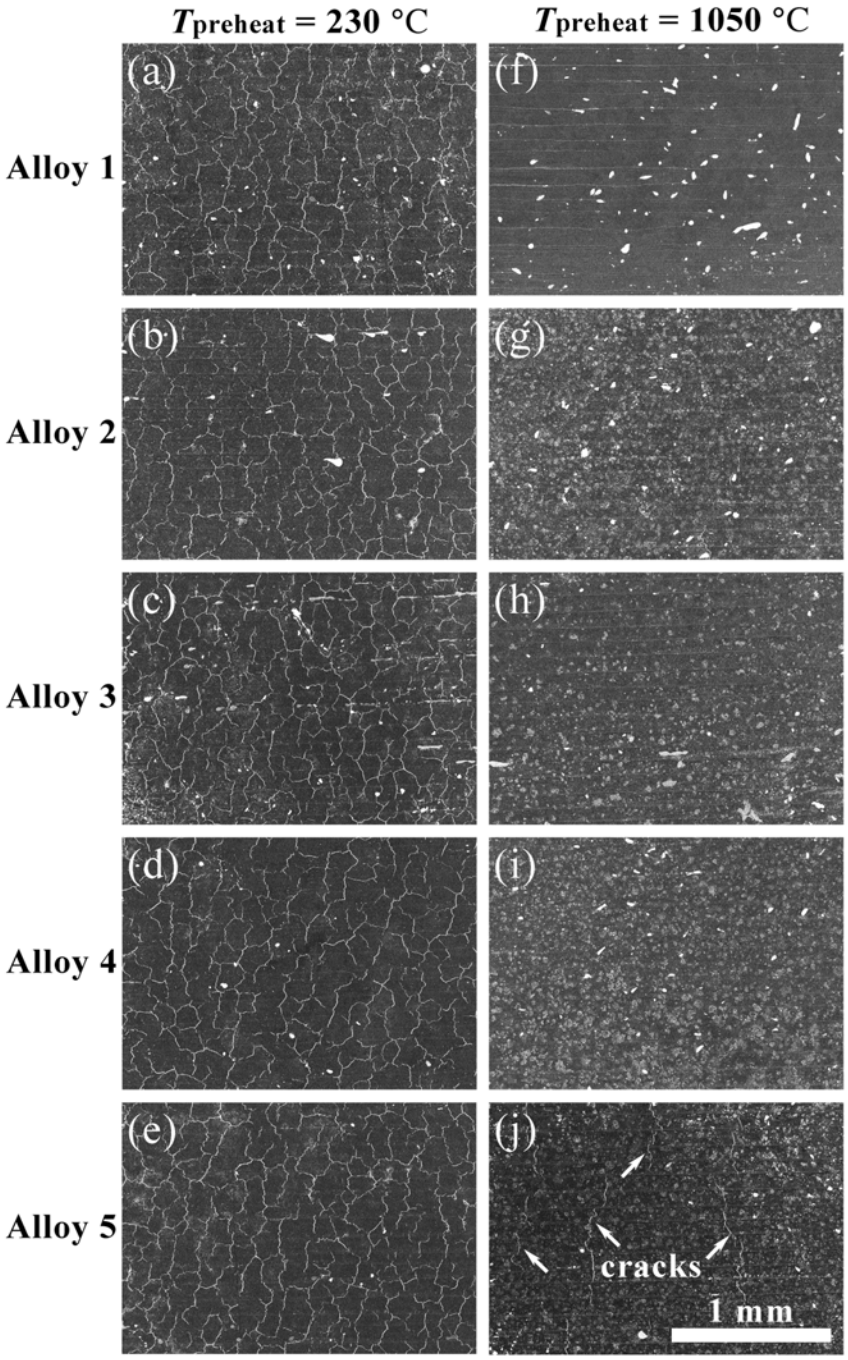

Fig. 8: SEM examination of the cracks as observed in the EB-PBF surface remelted samples (x-y plane): (a) to (e) preheat temperature of 230 °C; (f) to (j) preheat temperature of 1050 °C. Alloy IDs are indicated at the left of each row. Note the identified cracks are highlighted using bright-contrast outlines.

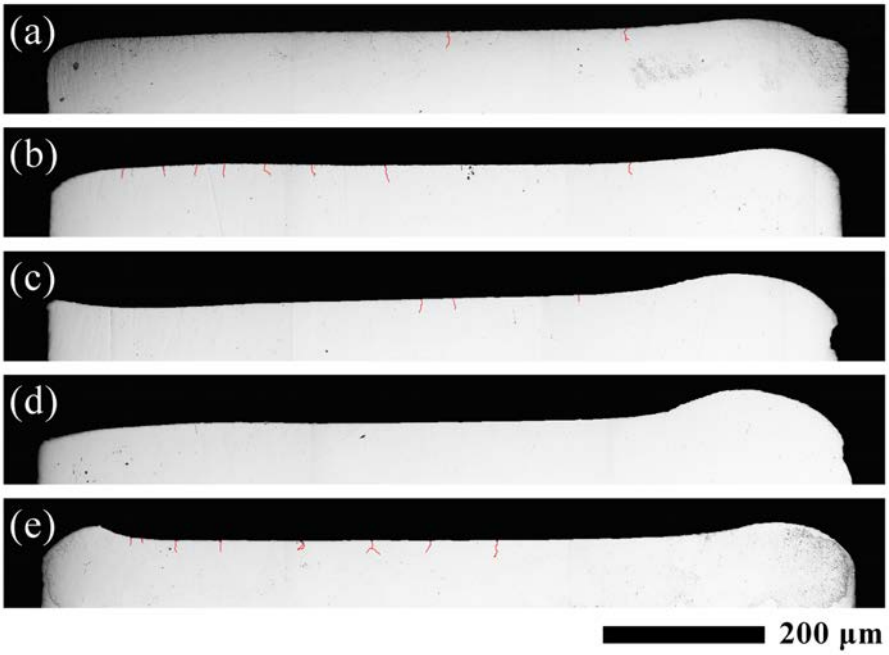

Fig. 9: Optical micrographs of the vertical section (x-z plane) of each sample: (a) to (e) alloys 1 to 5, respectively. All samples were subjected to surface remelting at the preheat temperature of 1050 ºC. Note the identified cracks are marked in red.

Fig. 10a to 10e show the equilibrium solidification paths as calculated with TCNI10 database of Thermo-Calc software. For each designed superalloy, there is no significant difference in solidification processes, i.e. all of them experience three solidification stages of L, L+γ, and L+γ+γ′. Alloy 4 exhibited a narrower freezing range and a smaller L+γ+γ′ zone when compared to the other alloys. Neither TCP phase nor carbide was observed at the end of solidification. To evaluate the accuracy of the thermodynamic calculation, SEM examination was conducted to reveal the microstructure details of alloys 1 to 5, as shown in Fig.10f to 10j. It is evident that neither the TCP phase nor carbide can be seen at the grain or dendritic boundary. This means that the M_d-based thermal stability prediction is accurate and reliable. Furthermore, the SEM study shows that alloys 1 and 4 have coarser columnar structures than alloys 2, 3 and 5. This means the predicted solidification curves are consistent with the experimental observation.

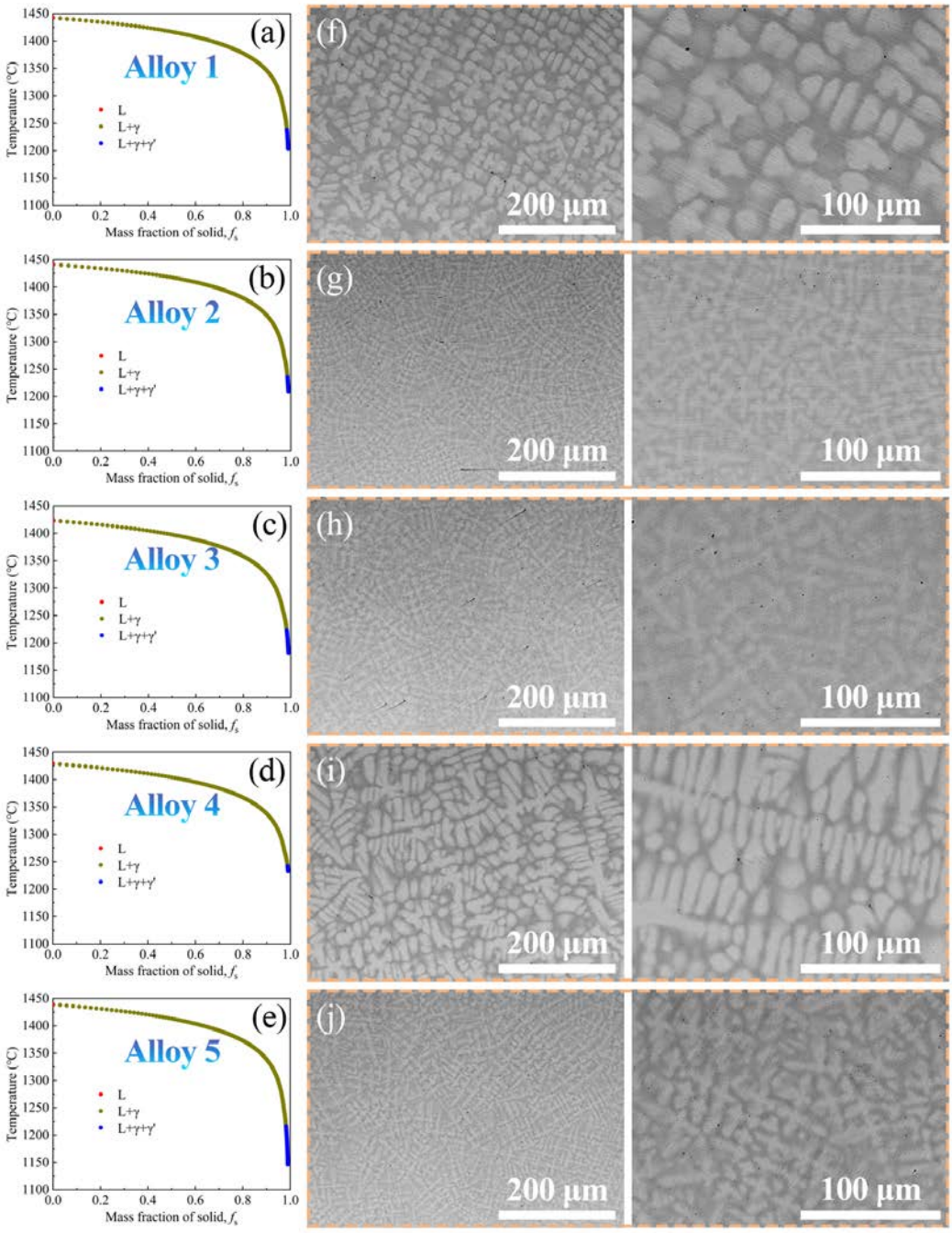

Fig. 10: (a-e) Equilibrium solidification curves for alloys 1 to 5; (f-j) SEM observations of alloys 1 to 5, with left column showing low-magnification images, while the right column showing the high-magnification images.

Two additional experimental verifications which were performed using the as-cast samples with the alloy compositions of alloys 1 to 5 are the measurement of mass density and determination of thermodynamic properties. Refer to Appendix A for the detail of experimental methods. It was confirmed that the Hull's regression equation and CALPHAD approach can be used to guide the alloy design in terms of the mass density, freezing temperature range and γ′ solvus temperature. Note such finding is

consistent with the previous studies with the examples of [55] for the density prediction and [3] for the phase-transformation temperature.

4.2 Bulk sample printing and material qualification

The rapid AM printability screening narrowed the list of alloy candidates down from five to one. The same EB-PBF machine was then used to fabricate bulk samples with nine cuboids (dimensions of 25×25×20 mm^3) per batch, as schematically shown in Fig. 11a. Alloy powders were prepared using the plasma rotating electrode processing (PREP) method, with their size distribution measured as 60.9 μm, 119.3 μm and 221.6 μm, for the respective D10, D50 and D90, using the laser diffraction method. For the bulk sample printing, beam power P of 600 W, scan speed v of 300 mm/s, line offset L_{off} of 0.1 mm, and preheat temperature of 1050 °C were chosen, together with the unidirectional scan strategy.

Fig. 11b shows the optical micrograph of alloy 4 in the as-built condition, revealing a virtually crack-free microstructure in the main body of the specimen, except for one crack at the very bottom (this region would be cut off in a real-word scenario). To fully recognise the excellent AM printability, an existing Ni-base superalloy René N5 type was chosen for making a direct comparison. Fig. 11c reveals the presence of several cracks in the as-built René N5 sample, and these large cracks extended almost half of the specimen. The EB-PBF alloy 4 sample was subjected to a full heat treatment, involving solution treating for 4 h at 1260 °C (oil quenched), followed by γ′-precipitate aging at 1050 °C for 8 h (oil quenched). The temperature selection was guided by the combination of differential scanning calorimetry measurement and CALPHAD thermodynamics calculation. Alloy 4 in as-built condition has a columnar dendrite structure with well-defined γ′-cuboids with size of ~92 nm, Fig. 11d. No secondary phase was found in the as-built condition. After solution treating and aging, chain-like Ta, Hf-rich carbides precipitated from the inter-dendritic region (Fig. 11e and 11f) according to energy-dispersive X-ray spectroscopy (EDS) mapping results, in alignment with our previous work [60].

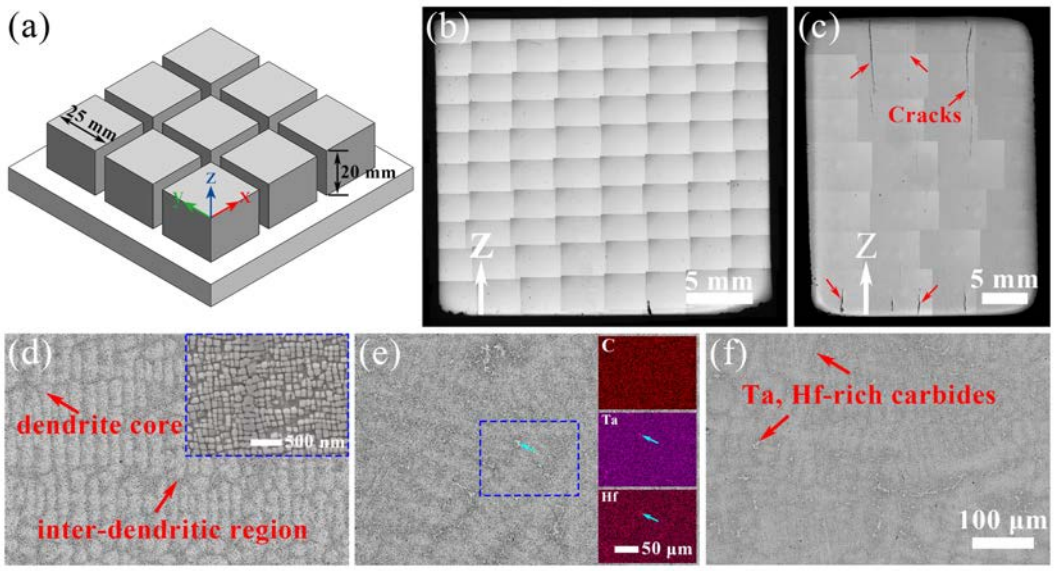

Fig. 11: (a) Schematic diagram of one batch of as-built alloy 4 samples; (b) and (c) comparison of the alloy 4 (crack-free) and a typical second-generation single-crystal Ni-base superalloy René N5 (the presence of cracks) as revealed under the optical microscopy. Both samples were printed using the same EB-PBF melt parameters (details can be found elsewhere [60]) and samples were polished down to 0.5 μm diamond paste prior to taking the images. Additional microstructure observations by using secondary electron SEM imaging mode were conducted on alloy 4: (d) as-built; (e) solution treated and (f) aged conditions.

Creep test of alloy 4 was performed on a SANS CMT504A1 tester, with the specimen dimensions of 10 mm in gauge length, 3 mm in width and 1 mm in thickness. Prior to the test, specimen surface was subjected to polishing down to 2000-grit SiC paper, followed by ethanol ultrasonic cleaning. Three thermocouples were attached onto the specimen near the top, middle and bottom to monitor the temperature. The specimen was heated to 980 ºC with the rate of 10 ºC/min, and then held at the temperature for 30 mins prior to applying the load of 120 MPa. During the entire creep test, the temperature variation was controlled within ±2 ºC. Fig. 12a presents the experimentally measured creep curve and the derived creep rate vs. time. Overall, the creep rupture time reaches 612 h which is comparable to the ANN model prediction of 603 h. Also, the minimum creep rate was determined as 4.39×10^{-5} h^{-1} (Fig. 12a).

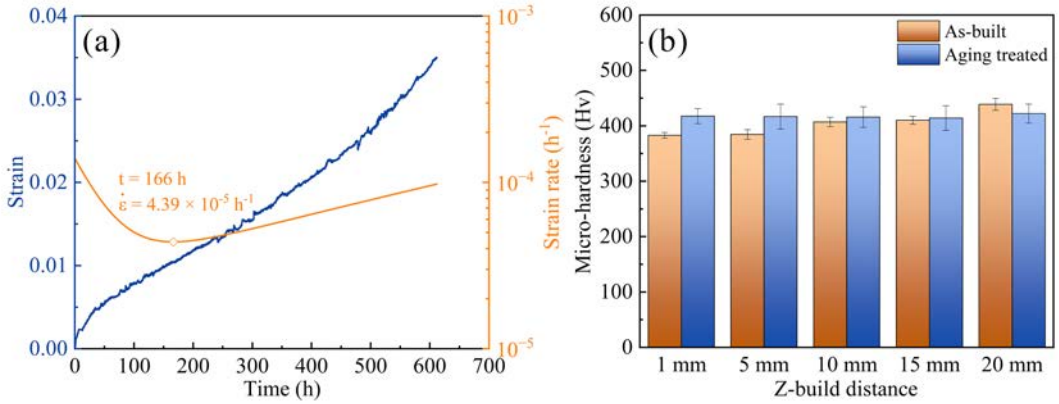

Fig. 12: (a) Creep curve of EB-PBF alloy 4 at 980 °C / 120 MPa, with the primary Y-axis indicating strain, while the secondary Y-axis indicating strain rate; (b) microhardness values of the as-built and fully heat-treated conditions of alloy 4 as measured at different build heights (Z=1 mm, 5 mm, 10 mm, 15 mm and 20 mm).

Vickers hardness measurements were performed on a FALCON511 micro-hardness tester, with the load of 200g and dwell time of 10s. Ten individual measurements per condition were made to derive the average value. Fig. 12b compares the as-built with fully heat-treated conditions of alloy 4. The Z-build variation was also measured as it provides important indication of the thermal stability. For the as-build condition, the micro-hardness was determined as 382.8±5.2, 384.5±8.8, 406.9±8.5, 410.1±7.1 and 438.9±10.8, for the Z-build height of 1 mm, 5 mm, 10 mm, 15 mm and 20 mm, respectively. This suggests coarsening of γ′-precipitate occurred towards the bottom of the sample build. However, when the samples were subjected to the heat treatment, the micro-hardness results suggested the more uniform distribution with the lowest value of 417.2±18.5 and highest value of 434.7±14.6 Hv.

5. Discussion

Finding the optimal alloy composition that best meets multiple criteria (or called as inequality constraints as stated in Table 1) represents a multi-objective optimisation problem, according to [61]. Multiple criteria come with additional degrees of freedom, and thus the utility function (U) can be introduced to combine the objectives into a single measure that reflects the overall quality of a solution. In the context of the present work, the alloy composition is the objective function, while SCMI, M_d value, density, etc. are a series of criteria (with each objective described by its objective function). Mathematically, the adopted approach can be summarised as weighted sum method:

$$U = \sum_{i=1}^{k} w_i Q_i(\mathrm{x}) \quad (8)$$

where U is the utility function, k is the number of objective functions, w_i is the weight, and $Q_i(\mathrm{x})$ is objective function. The objective functions $Q_i(\mathrm{x})$ are defined such that when a solution satisfies a certain criterion, $Q_i(\mathrm{x})=1$, and when it does not, $Q_i(\mathrm{x})=0$. In other words, a binary objective function ($Q_i(\mathrm{x})=1$ or $Q_i(\mathrm{x})=0$) is used, allowing for a simplification of the optimisation problem. All weights (w_i) are set to 1, indicating equal importance for all objectives. There are nine objective functions, as stated in Table 1, and thus k is equal to 9.

Apparently, the above-mentioned multi-objective optimisation method suits the purpose of the present work, because what concerned us the most from the perspective of alloy design is whether a criterion is met, rather than its specific values. For example, if a designed superalloy meets the density criterion of ρ<9.1 g/cm^3, $Q_i(\mathrm{x})=1$ will be assigned. The specific value for the density becomes not relevant from the perspective of binary indicator.

Through the integration of computational alloy design and rapid AM printability screening experimental validation, a new Ni-base superalloy has been developed to meet target specifications as outlined in Table 1. In terms of the AM printability, both the freezing temperature range (as well as the crack susceptibility index) and SCMI factor have been considered via the modelling approach. However, this does not necessarily guarantee a crack-free microstructure as revealed by the surface remelting experiment, where only alloy 4 is proven as immune to cracking (Fig. 8 and Fig. 9). The remaining four alloys all showed some level of cracking, despite the high build temperature of 1050 ºC which helped to prevent cracking. Given the small difference in terms of the model predicted SCMI (5.52 to 5.81 wt.%), crack susceptibility index (973 to 1162 °C) and freezing temperature range (104 to 154 °C) for the top five alloy compositions, it is important to emphasise the need for performing experimental verification. To this end, the surface remelting strategy (Fig. 7) brings out a clear benefit in terms of cost saving, representing a new rapid printability screening method. The present work demonstrates the efficacy of this method, which can be used to replace the production of AM powders with five different compositions for the purposes of printing the bulk sample.

Part of the motivation behind the present work is to ensure the good AM printability does not sacrifice the creep property. Therefore, the ML method has been

602 employed to forecast the creep performance, instead of conducting a batch of creep tests
603 which are known to be costly and time consuming. ML is an emerging technique, and
604 several ML methods were employed for predicting the creep rupture time, such as RF,
605 SVR, gaussian process regression (GPR), lasso regression (LR), ridge regression (RR),
606 gradient boosted tree (GBT), and deep neural network (DNN). Liu et al. [17] compared
607 five of them, including RF, SVR, GPR, LR and RR, to reveal the differences in creep
608 mechanisms of alloy samples in different clusters. Sanchez et al. [62] determined the
609 main influencing factors on creep rates in L-PBF Alloy 718 by using ML methods of
610 RF, GBT, SVR, DNN, RR and LR, together with the input data of several build
611 parameters and geometrical material descriptors. Furthermore, ANN has been proven
612 as a reliable method to predict the creep life of alloys processed by conventional means
613 [63,64]. To this end, the present work represents the first attempt of using ANN method
614 to predict the creep rupture time of AM Ni-base superalloy. It turns out to be a success
615 in terms of achieving the good agreement between the experimental data (612 h) and
616 modelling prediction (603 h). Moreover, there is no reason to believe that such a good
617 agreement is only applicable to the chosen creep condition of 980°C/120 MPa. This is
618 because the ANN model (Fig. 4b) is characterised by the low RMSE of 40.2 h and low
619 MAE of 19.8 h, as well as the high R^2 of 0.98 (Fig. 4a). Despite the success, nearly all
620 ML methods (e.g., ANN) are recognised as the "black box" in nature. This means
621 whether the model has achieved good results would also rely on its interpretability.
622 Chen et al. [65] found that adding minor Ti (~0.5 wt.%) to a second-generation
623 single-crystal Ni-base superalloy can greatly improve the creep rupture time by more
624 than twice compared to René N5 (45 h vs. 100 h at 1030 °C / 230 MPa), and the Ti
625 concentration is close to alloy 4. Kalyanasundaram et al. [66] prepared crack-free
626 CM247LC alloy via L-PBF, with the rupture time at 800 °C of ~200 h at 500 MPa, 65
627 h at 550 MPa, 30 h at 600 MPa. However, carbides with enrichments of Ti/Hf/Ta/W/C
628 elements can be observed in the as-fabricated state compared with the current work in
629 Fig. 10d, 10i and 11d. This indicates that alloy 4 has a good thermal stability thanks to
630 the high accuracy of M_d predictions.
631 The correlation between each pair of features is visualised via the heatmap of
632 Fig. 13. It reveals that element such as Al and Ta, especially the former, exhibits
633 statistically significant positive correlations with γ′ content. This finding aligns with
634 their metallurgical role as the primary forming element for the γ′ precipitate. Moreover,

the γ′ content demonstrates a strong positive correlation with creep rupture time, with W and Cr following closely. On the other hand, Ni consistently exhibits negative correlations with most of the other elements. Importantly, no notably strong correlation was observed between any two elements. This observation suggests that these elements should be retained simultaneously as input data, emphasising their individual contributions without significant multicollinearity.

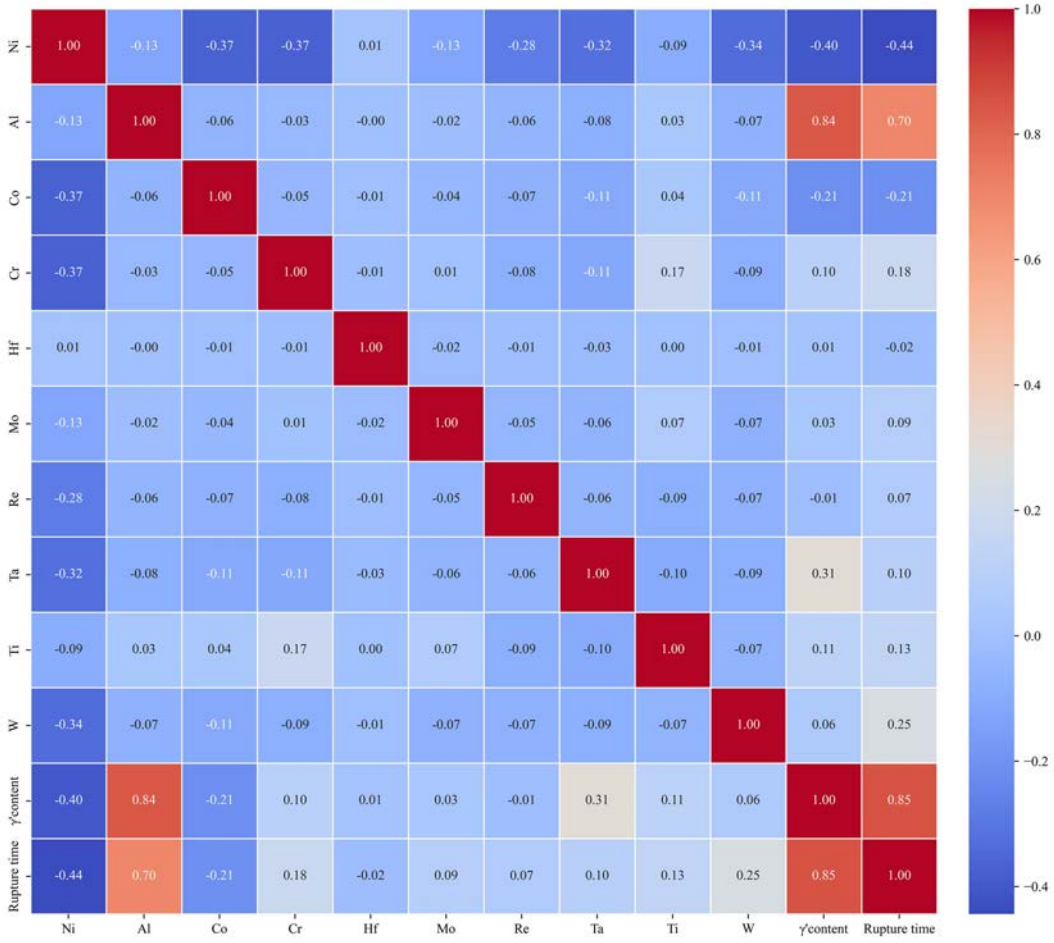

Fig. 13: Heatmap visualisation of the correlation between every pair of features as well as the target (note that the colour intensity and numerical values in each cell indicating the strength of correlation between the corresponding features).

Fig. 14 explores the linear relationship between each alloying element and the creep rupture time. γ′ content and Al exhibit a positive correlation and Ni shows a negative correlation, establishing clear linear relationships with the target. By comparison, other elements display less discernible linear patterns (consistent with Fig. 13). This observation explains why the accuracy of the SVR with a linear kernel (Fig. 4d) is comparatively lower than other ML algorithms. Therefore, we opted not to consider simple linear regression and logistic regression in this study.

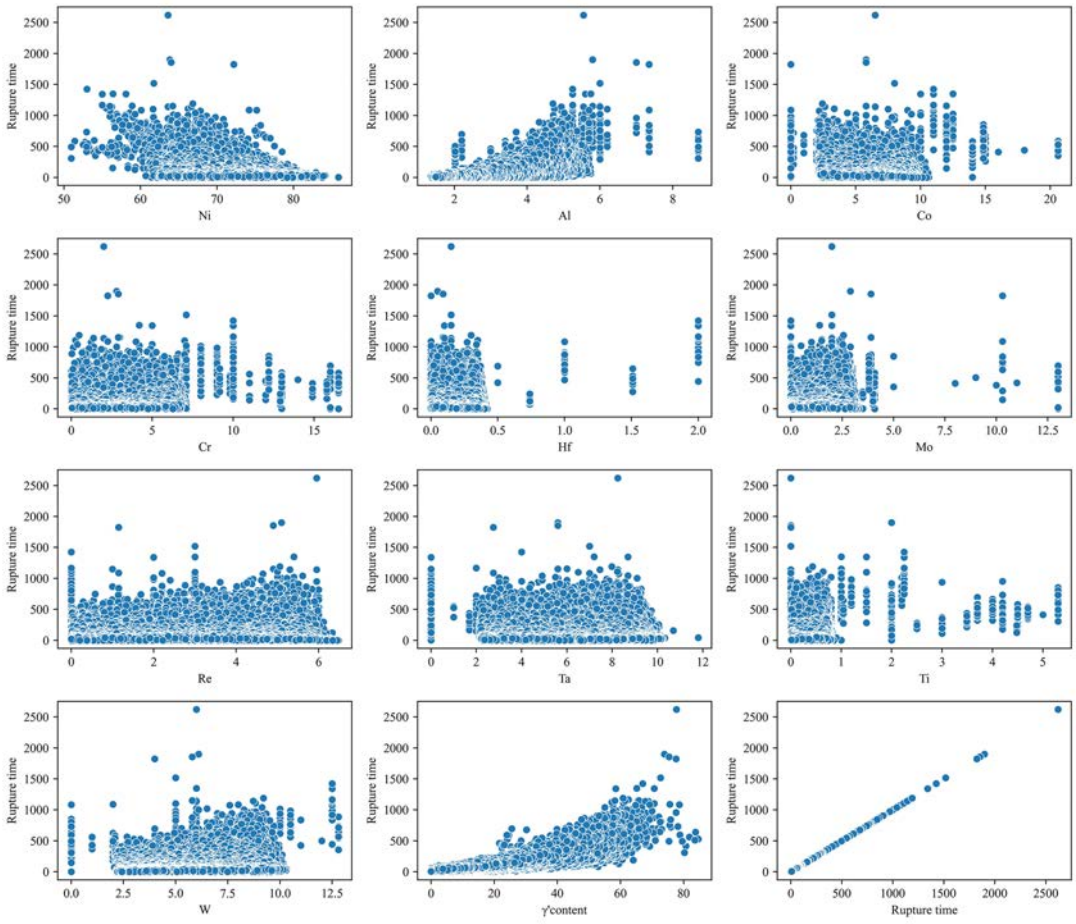

Fig. 14: Scatter matrix for the relationship between the alloying features and the target.

Now let's consider the interpretability of the ANN model. The interpretability analysis was performed using the local interpretable model-agnostic explanations (LIME) method [67], aimed to evaluating whether the model has truly learned useful functional relationships. The idea behind the LIME is to approximate the nonlinear function learned by a ML model to a linear function within a small neighbourhood of an individual sample (i.e., a specific element type). In practice, this is achieved by generating a small set of samples around the sample of interest, obtaining their predicted outcomes (i.e., creep life) using the ANN model, and finally performing the simple linear regression. The interpretability analysis results for the 10 element types and γ′-volume fraction (in total 11 features) are presented in Fig. 15. In the bar chart, the positive direction (pointing right) of each reference bar indicates a positive effect on creep life (leading to increased rupture time). Likewise, the negative direction suggests such feature would cause a decreased creep rupture time. The bar length

indicates the feature weight. Five alloys are considered separately, Fig. 15a to 15e in order of alloy 1 to 5, and the analysis results are overall consistent.

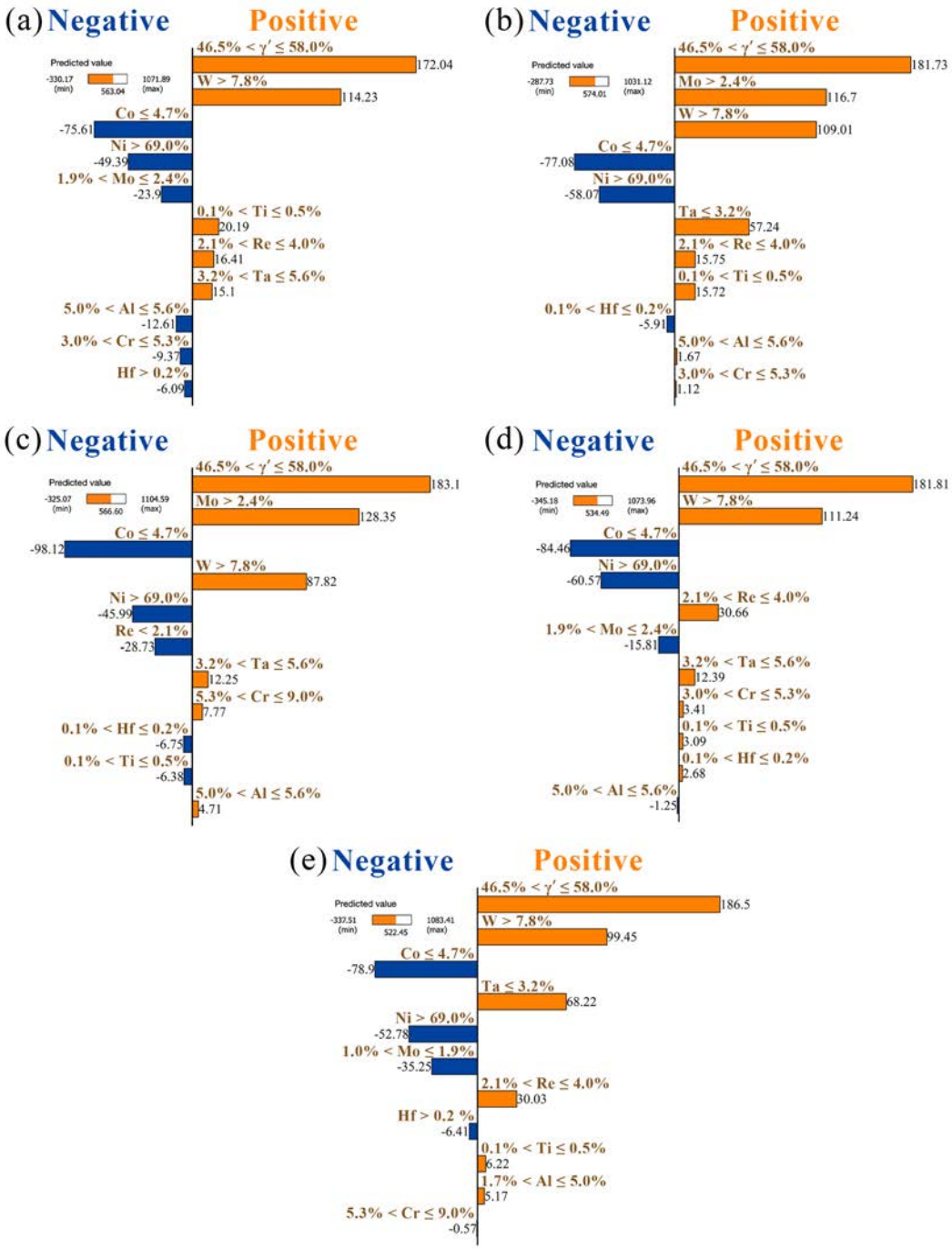

Fig. 15: Analysis of interpretability of ANN model using the LIME method: (a) to (e) alloy 1 to 5, illustrating the influence of feature weight on creep rupture time.

The LIME analysis shows that the γ′-volume fraction within the data range of 46.5% to 58.0% (with reference to the set target of >50%) would impact positively the creep rupture time. By incorporating the γ′-volume fraction as an input feature to the ANN model, the contributions of Al, Ti and Ta are reduced to a very low positive value

682 or even towards a low negative value. This is as expected because they are all γ′-forming
683 elements [28], namely, their influence on the creep rupture time has been already
684 considered by the feature of γ′-volume fraction. The second key learning outcome is
685 the role of W > 7.8%, which has a positive effect on creep life. W is one of the most
686 effective solid solution strengthening elements in Ni-base superalloys, and research
687 conducted by Zenk et al. [68] revealed that the higher W content led to reduced
688 secondary creep rate. Furthermore, two out of the five alloys (i.e., alloy 2 and 3 in Fig.
689 14b and 14c) suggest that Mo content of > 2.4% generates a positive impact on creep
690 rupture time. This seems to agree with the experimental observation by Zhang et al.
691 [69], where the increased ratio of Mo to W resulted in the prolonged creep life. Note
692 that the LIME analysis could not cope with synergistic effect in a sense of treating
693 combined feature effect. In addition, Re in the range from 2.1% to 4.0% would have a
694 positive influence on creep life. This agrees with the metallurgical role of Re in terms
695 of its enrichment at partial dislocations, imposing a drag effect on dislocation
696 movement [70]. Moreover, the LIME analysis shows that Co content of ≤ 4.7% would
697 generate the negative influence. In other words, by increasing the Co content of higher
698 than this critical concentration, one would expect an increased creep rupture time. This
699 seems to concur with our consensus that Co in Ni-base superalloys plays a vital role on
700 the enhanced creep properties because it can increase γ′-volume fraction and reduce the
701 stacking fault energy [71]. To summarise, based on the LIME analysis, the present
702 ANN model shows a good level of reliability in a sense that it did truly learn meaningful
703 functional relationships.
704 The LIME analysis is also in line with the trend of alloy development.
705 Experience has shown that improvements in creep strengthening occur in the increasing
706 order of Co→Cr→Ta→W→Re [28]. Although Re has a significant effect on the creep
707 performance improvement, excessive addition will promote the precipitation of
708 intermetallic phases (such as the TCP phases), by lowering the thermal stability (refer
709 to the high M_d value of Re, 1.267 eV). However, the range of Re among five designed
710 alloys is still within the scope of the second-generation single-crystal Ni-base
711 superalloy. Lowering the content of Cr and Ta is another trend from the development
712 of second- to the fourth-generation single-crystal Ni-base superalloys. This is broadly
713 consistent with the composition as shown in Table 3 (comparing with other second-
714 generation single-crystal Ni-base superalloys such as René N5). Increasing the W

content to a high level (over 8.5 wt.%) to offset the decrease in other elements might have a positive effect, although the specific mechanism for such a large amount of W is still unknown except for the results of LIME.

Acknowledging the limitations of the ANN model is equally important. Its design doesn't aim to indicate any specific physical relationships, but rather provides an alternative means to predict results similar to physical constitutive laws. It becomes particularly robust when the model includes adequate physics-related input features. The above-mentioned interpretability analysis serves to compare the variable importance against our state-of-the-art field knowledge. This should not be misunderstood with the discovery of any new physical relationships. Numerous physical creep models, outlined in the open literature e.g., [30,72–74], have established the links between controlling microstructural features and creep life by precisely accounting for underlying deformation and damage processes. However, their applicability is predominantly limited to certain stress and temperature conditions as well as the material process history. When addressing the complexity of various alloying elements and multiple parameters during AM, these models achieved limited success. It was reported in [17] that when considering the microstructural evolution information in a data-driven models, a more accurate prediction result of creep rupture time can be obtained, when compared to the use of physical models. Therefore, the use of ANN approach becomes notably appealing in scenarios where intricate physical processes pose challenges for conventional physics-based methodologies [75].

Feature correlation is another method to help understand the ML predicted results. Here, both the Pearson correlation coefficient (PCC) and maximum information coefficient (MIC) were used to characterise the feature correlation of the ANN model. The PCC is the most common way of measuring the strength and direction of the linear correlation between two variables [76], whereas the MIC can provide a measure of the strength of the linear or nonlinear correlation [77]. The value range of the PCC is [-1,1], suggesting a strong positive correlation if its value becomes close to 1, while a strong negative correlation for a value of close to -1. The value range of the MIC is [0,1], suggesting a strong correlation between two variables, when its value becomes close to 1, regardless of linear or non-linear relationship.

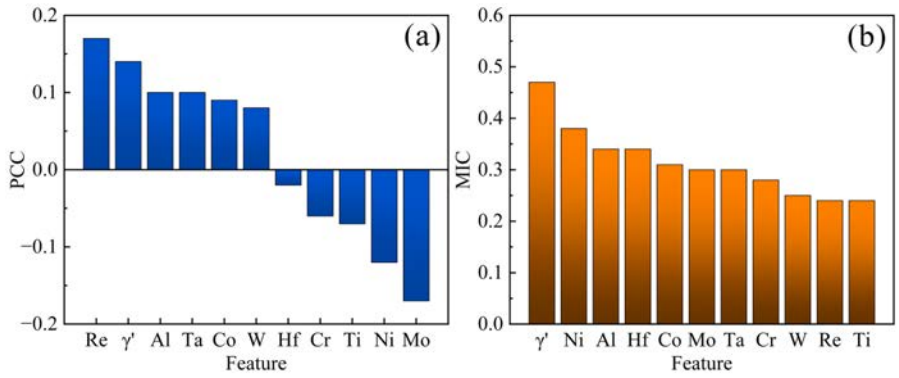

Fig. 16: Feature correlation related to the creep rupture time based on the PCC in (a) and MIC in (b).

The PCC and MIC evaluation results for 10 elements plus the γ′ content (i.e., in total 11 input features) are shown in Fig. 16a and 16b. There is no strong correlation between each feature and the predicted creep life, suggesting a very weak linear relationship between the two variables. However, the PCC evaluation does reveal some positive correlation of key elements, γ′ content and the creep life. For example, Re, Al, Ta, Co and W elements in Ni-base superalloys are known to be beneficial for the creep property [28,68–70]. In terms of the MIC evaluation, γ′ content was found to have a value of ~0.5, suggesting a strong correlation between this feature and creep life. By contrast, all the elements do not show a strong correlation, which suggests that microstructure (e.g., γ′ content) plays a more important role when compared to the alloy composition. Based on the PCC and MIC analyses of the ANN model prediction, it seems that introducing other input features which can represent the microstructure-property interrelationship might generate an even more reliable prediction. It has been recognised in literature that microstructure feature such as grain size [78,79], stacking fault energy [80], diffusion coefficient of γ or γ′-forming elements [81], and AM parameters [82] all play an important role on the creep property. Using a thermodynamic calculation software (e.g., Thermo-Calc) to calculate these parameters is a viable route.

6. Conclusions

The following conclusions can be drawn from this work:

1) Using the integrated computational tools coupled with rapid AM printability screening experimental methods, a new Ni-base superalloy

composition (Ni-5.03Al-2.69Co-5.63Cr-0.04Hf-1.91Mo-2.36Re-3.32Ta-0.57Ti-8.46W-0.05C-0.019B) is proposed to meet four design criteria of AM printability, creep, thermal stability and density.

2) Surface remelting strategy is proven as an effective means to examine the AM printability in a cost-effective manner, and this new rapid printability screening method provides a bypass as far as the expensive AM powder production in significant quantities is concerned.

3) Among the five ML algorithms considered, ANN shows the highest prediction accuracy in the context of comparing the experimental measured with model predicted creep life. The measured creep life of 612 h is close to the model predicted 603 h.

4) LIME-based interpretability analysis substantiates that the ANN model truly learns meaningful functional relationships between input features and the output. PCC and MIC-based evaluation emphasises the importance of incorporating microstructure-related input feature as it plays a key role on the prediction results and reliability.

Acknowledgement

Bo Chen acknowledges financial supports by the UK's Engineering and Physical Sciences Research Council, EPSRC First Grant Scheme EP/P025978/1 and Early Career Fellowship Scheme EP/R043973/1. Hui Peng acknowledges financial support from National Natural Science Foundation of China (52071006). In addition, Bo Chen extends his sincere thank you to Prof. Shengkai Gong, Beihang University, who initiated the research collaboration.

Appendix A: Density measurement and determination of phase transformation temperatures

Using the cast samples with compositions of alloy 1 to 5, the mass density was measured by using Archimedes drainage method. Five measurements were taken per alloy type, and the averaged value of mass density was determined as 8.85, 8.88, 8.63, 8.82, 8.88 g/cm^3, in order of alloy 1 to 5. By comparison, the Hull's model (Eq. 7) predicted values were 9.09, 9.09, 8.98, 8.98, 9.09 g/cm^3, respectively. The lower value

of the predicted density as compared to the measurement is as expected given the fact of first, k factor with a value of greater than 1 (Fig. 6b), and second, no consideration of the atom mixing.

A synchronous thermal analyser NETZSCH STA 449 F3 filled with argon was used to measure thermodynamic properties. The heating rate was set as 5 °C/min. The size of each test sample was 4 mm in diameter and 0.8 mm thick. By analysing the differential scanning calorimetry (DSC) data curve, for alloys 1 to 5 as shown in Fig. A1, the liquidus and solidus temperatures (T_L and T_S) as well as the γ′ solvus temperatures ($T_{\gamma'}$) of all five alloys were obtained. By comparison with the CALPHAD approach predicted values (Table A1), it seems that the model prediction shows a reasonably good agreement with experimental data.

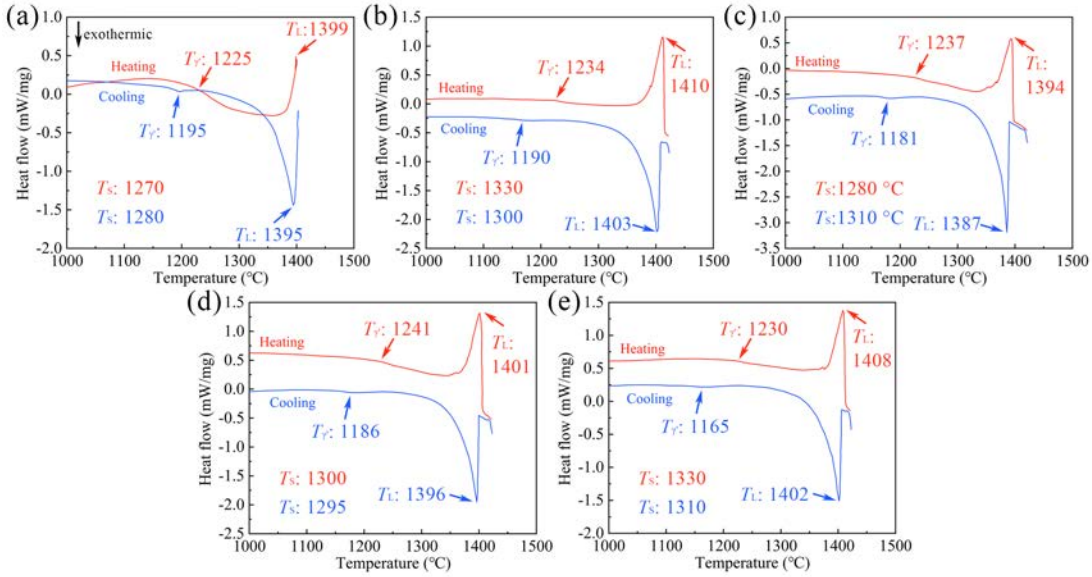

Fig. A1: Differential scanning calorimetry (DSC) curves obtained from alloys 1 to 5, during heating and cooling at 5 K/min, as presented in (a) to (e), respectively.

Table A1: Comparison of CALPHAD approach predicted thermodynamic properties with the DSC measured values for alloys 1 to 5. Note: freezing temperature range is the difference between T_L and T_s.

Alloy type	CALPHAD (ºC)			DSC (ºC)		
	T_L	T_S	Freezing range	T_L	T_S	Freezing range
Alloy 1	1418	1264	154	1399	1270	129
Alloy 2	1415	1296	119	1410	1330	80
Alloy 3	1401	1297	104	1394	1280	114
Alloy 4	1406	1299	107	1401	1300	101
Alloy 5	1421	1310	111	1408	1330	78

References

[1] Z. Rao, P.Y. Tung, R. Xie, Y. Wei, H. Zhang, A. Ferrari, T.P.C. Klaver, F. Körmann, P.T. Sukumar, A. Kwiatkowski da Silva, Y. Chen, Z. Li, D. Ponge, J. Neugebauer, O. Gutfleisch, S. Bauer, D. Raabe, Machine learning–enabled high-entropy alloy discovery, Science (1979) 378 (2022) 78–85. https://doi.org/10.1126/science.abo4940.

[2] S.P. Murray, K.M. Pusch, A.T. Polonsky, C.J. Torbet, G.G.E. Seward, N. Zhou, S.A.J. Forsik, P. Nandwana, M.M. Kirka, R.R. Dehoff, W.E. Slye, T.M. Pollock, A defect-resistant Co–Ni superalloy for 3D printing, Nat Commun 11 (2020) 4975. https://doi.org/10.1038/s41467-020-18775-0.

[3] Y.T. Tang, C. Panwisawas, J.N. Ghoussoub, Y. Gong, J.W.G. Clark, A.A.N. Németh, D.G. McCartney, R.C. Reed, Alloys-by-design: Application to new superalloys for additive manufacturing, Acta Mater 202 (2021) 417–436. https://doi.org/10.1016/j.actamat.2020.09.023.

[4] J. Li, K. Lim, H. Yang, Z. Ren, S. Raghavan, P.Y. Chen, T. Buonassisi, X. Wang, AI applications through the whole life cycle of material discovery, Matter 3 (2020) 393–432. https://doi.org/10.1016/j.matt.2020.06.011.

[5] A. Agrawal, A. Choudhary, Perspective: Materials informatics and big data: Realization of the “fourth paradigm” of science in materials science, APL Mater 4 (2016) 053208. https://doi.org/10.1063/1.4946894.

[6] C. Wang, C. Shen, C. Zhang, Y. Zhao, W. Xu, Tensile property prediction by feature engineering guided machine learning in reduced activation ferritic/martensitic steels, Journal of Nuclear Materials 535 (2020) 152208. https://doi.org/10.1016/j.jnucmat.2020.152208.

[7] C. Shen, C. Wang, X. Wei, Y. Li, S. van der Zwaag, W. Xu, Physical metallurgy-guided machine learning and artificial intelligent design of ultrahigh-strength stainless steel, Acta Mater 179 (2019) 201–214. https://doi.org/10.1016/j.actamat.2019.08.033.

[8] A. Agrawal, P.D. Deshpande, A. Cecen, G.P. Basavarsu, A.N. Choudhary, S.R. Kalidindi, Exploration of data science techniques to predict fatigue strength of steel from composition and processing parameters, Integr Mater Manuf Innov 3 (2014) 90–108. https://doi.org/10.1186/2193-9772-3-8.

[9] J. Wang, Y. Fa, Y. Tian, X. Yu, A machine-learning approach to predict creep properties of Cr–Mo steel with time-temperature parameters, Journal of Materials Research and Technology 13 (2021) 635–650. https://doi.org/10.1016/j.jmrt.2021.04.079.

[10] T. Sourmail, H.K.D.H. Bhadeshia, D.J.C. MacKay, Neural network model of creep strength of austenitic stainless steels, Materials Science and Technology 18 (2002) 655–663. https://doi.org/10.1179/026708302225002065.

[11] J.J. Möller, W. Körner, G. Krugel, D.F. Urban, C. Elsässer, Compositional optimization of hard-magnetic phases with machine-learning models, Acta Mater 153 (2018) 53–61. https://doi.org/10.1016/j.actamat.2018.03.051.

[12] D. Xue, D. Xue, R. Yuan, Y. Zhou, P. V. Balachandran, X. Ding, J. Sun, T. Lookman, An informatics approach to transformation temperatures of NiTi-based shape memory alloys, Acta Mater 125 (2017) 532–541. https://doi.org/10.1016/j.actamat.2016.12.009.

[13] L. Ward, S.C. O’Keeffe, J. Stevick, G.R. Jelbert, M. Aykol, C. Wolverton, A

machine learning approach for engineering bulk metallic glass alloys, Acta Mater 159 (2018) 102–111. https://doi.org/10.1016/j.actamat.2018.08.002.
[14] G.X. Gu, C.T. Chen, M.J. Buehler, De novo composite design based on machine learning algorithm, Extreme Mech Lett 18 (2018) 19–28. https://doi.org/10.1016/j.eml.2017.10.001.
[15] B.D. Conduit, N.G. Jones, H.J. Stone, G.J. Conduit, Design of a nickel-base superalloy using a neural network, Mater Des 131 (2017) 358–365. https://doi.org/10.1016/j.matdes.2017.06.007.
[16] D. Shin, Y. Yamamoto, M.P. Brady, S. Lee, J.A. Haynes, Modern data analytics approach to predict creep of high-temperature alloys, Acta Mater 168 (2019) 321–330. https://doi.org/10.1016/j.actamat.2019.02.017.
[17] Y. Liu, J. Wu, Z. Wang, X.G. Lu, M. Avdeev, S. Shi, C. Wang, T. Yu, Predicting creep rupture life of Ni-based single crystal superalloys using divide-and-conquer approach based machine learning, Acta Mater 195 (2020) 454–467. https://doi.org/10.1016/j.actamat.2020.05.001.
[18] M. Montakhab, E. Balikci, Integrated computational alloy design of nickel-base superalloys, Metallurgical and Materials Transactions A 50 (2019) 3330–3342. https://doi.org/10.1007/s11661-019-05252-7.
[19] H. Zhang, H. Fu, X. He, C. Wang, L. Jiang, L.-Q. Chen, J. Xie, Dramatically enhanced combination of ultimate tensile strength and electric conductivity of Alloys via Machine Learning Screening, Acta Mater 200 (2020) 803–810. https://doi.org/10.1016/j.actamat.2020.09.068.
[20] S. Si, B. Fan, X. Liu, T. Zhou, C. He, D. Song, J. Liu, Study on strengthening effects of Zr-Ti-Nb-O alloys via high throughput powder metallurgy and data-driven machine learning, Mater Des 206 (2021) 109777. https://doi.org/10.1016/j.matdes.2021.109777.
[21] F. Liu, Z. Wang, Z. Wang, J. Zhong, L. Zhao, L. Jiang, R. Zhou, Y. Liu, L. Huang, L. Tan, Y. Tian, H. Zheng, Q. Fang, L. Zhang, L. Zhang, H. Wu, L. Bai, K. Zhou, High‐throughput method–accelerated design of Ni-based superalloys, Adv Funct Mater 32 (2022). https://doi.org/10.1002/adfm.202109367.
[22] C. Körner, Additive manufacturing of metallic components by selective electron beam melting — a review, International Materials Reviews 61 (2016) 361–377. https://doi.org/10.1080/09506608.2016.1176289.
[23] Y. Li, W. Kan, Y. Zhang, M. Li, X. Liang, Y. Yu, F. Lin, Microstructure, mechanical properties and strengthening mechanisms of IN738LC alloy produced by Electron Beam Selective Melting, Addit Manuf 47 (2021) 102371. https://doi.org/10.1016/j.addma.2021.102371.
[24] M. Ramsperger, R.F. Singer, C. Körner, Microstructure of the Nickel-base superalloy CMSX-4 fabricated by selective electron beam melting, Metallurgical and Materials Transactions A 47 (2016) 1469–1480. https://doi.org/10.1007/s11661-015-3300-y.
[25] S. Kou, A criterion for cracking during solidification, Acta Mater 88 (2015) 366–374. https://doi.org/10.1016/j.actamat.2015.01.034.
[26] Y. Yao, C. Xing, H. Peng, H. Guo, B. Chen, Solidification microstructure and tensile deformation mechanisms of selective electron beam melted Ni3Al-based alloy at room and elevated temperatures, Materials Science and Engineering: A 802 (2021) 140629. https://doi.org/10.1016/j.msea.2020.140629.
[27] L. Tan, X. Ouyang, L. Ye, H. Dong, X. Xiao, J. Su, L. Huang, F. Liu, Synchronously enhanced printability and properties of additively manufactured nickel-based superalloys via alloying minor Sc, Journal of Materials Research

and Technology 30 (2024) 890–893. https://doi.org/10.1016/j.jmrt.2024.03.087.
[28] R.C. Reed, The superalloys: Fundamentals and applications, Cambridge University Press, London, 2006. https://doi.org/10.1017/CBO9780511541285.
[29] K. Xu, G. Wang, J. Liu, J. Li, J. Liu, X. Wang, Y. Yang, L. Ye, Y. Zhou, X. Sun, Creep behavior and a deformation mechanism based creep rate model under high temperature and low stress condition for single crystal superalloy DD5, Materials Science and Engineering: A 786 (2020) 139414. https://doi.org/10.1016/j.msea.2020.139414.
[30] A. Epishin, T. Link, Mechanisms of high-temperature creep of nickel-based superalloys under low applied stresses, Philosophical Magazine 84 (2004) 1979–2000. https://doi.org/10.1080/14786430410001663240.
[31] K. Kakehi, S. Banoth, Y.L. Kuo, S. Hayashi, Effect of yttrium addition on creep properties of a Ni-base superalloy built up by selective laser melting, Scr Mater 183 (2020) 71–74. https://doi.org/10.1016/j.scriptamat.2020.03.014.
[32] C. Körner, M. Ramsperger, C. Meid, D. Bürger, P. Wollgramm, M. Bartsch, G. Eggeler, Microstructure and mechanical properties of CMSX-4 Single crystals prepared by additive manufacturing, Metallurgical and Materials Transactions A 49 (2018) 3781–3792. https://doi.org/10.1007/s11661-018-4762-5.
[33] P. Wollgramm, D. Bürger, A.B. Parsa, K. Neuking, G. Eggeler, The effect of stress, temperature and loading direction on the creep behaviour of Ni-base single crystal superalloy miniature tensile specimens, Materials at High Temperatures 33 (2016) 346–360. https://doi.org/10.1080/09603409.2016.1186414.
[34] D. Bürger, A.B. Parsa, M. Ramsperger, C. Körner, G. Eggeler, Creep properties of single crystal Ni-base superalloys (SX): A comparison between conventionally cast and additive manufactured CMSX-4 materials, Materials Science and Engineering: A 762 (2019) 138098. https://doi.org/10.1016/j.msea.2019.138098.
[35] Materials Scientific Data Sharing Network, Http://Www.Materdata.Cn (n.d.).
[36] National Institute for Materials Science, Https://Www.Nims.Go.Jp (n.d.).
[37] L. Breiman, Random forests, Mach Learn 45 (2001) 5–32. https://doi.org/10.1023/A:1010933404324.
[38] M. Awad, R. Khanna, Support Vector Regression, in: Efficient learning machines, Apress, Berkeley, CA, 2015: pp. 67–80. https://doi.org/10.1007/978-1-4302-5990-9_4.
[39] D.P. Kingma, J. Ba, Adam: A Method for stochastic optimization, (2014).
[40] N.J. Harrison, I. Todd, K. Mumtaz, Reduction of micro-cracking in nickel superalloys processed by selective laser melting: A fundamental alloy design approach, Acta Mater 94 (2015) 59–68. https://doi.org/10.1016/j.actamat.2015.04.035.
[41] D. Tomus, P.A. Rometsch, M. Heilmaier, X. Wu, Effect of minor alloying elements on crack-formation characteristics of Hastelloy-X manufactured by selective laser melting, Addit Manuf 16 (2017) 65–72. https://doi.org/10.1016/j.addma.2017.05.006.
[42] J.N. Ghoussoub, P. Klupś, W.J.B. Dick-Cleland, K.E. Rankin, S. Utada, P.A.J. Bagot, D.G. McCartney, Y.T. Tang, R.C. Reed, A new class of alumina-forming superalloy for 3D printing, Addit Manuf 52 (2022) 102608. https://doi.org/10.1016/j.addma.2022.102608.
[43] N. Zhou, A.D. Dicus, S.A.J. Forsik, T. Wang, G.A. Colombo, M.E. Epler, Development of a new alumina-forming crack-resistant High-γ′ fraction Ni-Base

superalloy for additive manufacturing, in: 2020: pp. 1046–1054. https://doi.org/10.1007/978-3-030-51834-9_102.
[44] E. Chauvet, P. Kontis, E.A. Jägle, B. Gault, D. Raabe, C. Tassin, J.J. Blandin, R. Dendievel, B. Vayre, S. Abed, G. Martin, Hot cracking mechanism affecting a non-weldable Ni-based superalloy produced by selective electron Beam Melting, Acta Mater 142 (2018) 82–94. https://doi.org/10.1016/j.actamat.2017.09.047.
[45] A. Després, S. Antonov, C. Mayer, C. Tassin, M. Veron, J.J. Blandin, P. Kontis, G. Martin, On the role of boron, carbon and zirconium on hot cracking and creep resistance of an additively manufactured polycrystalline superalloy, Materialia (Oxf) 19 (2021) 101193. https://doi.org/10.1016/j.mtla.2021.101193.
[46] T.J. Garosshen, T.D. Tillman, G.P. McCarthy, Effects of B, C, and Zr on the structure and properties of a P/M nickel base superalloy, Metallurgical Transactions A 18 (1987) 69–77. https://doi.org/10.1007/BF02646223.
[47] J. Grodzki, N. Hartmann, R. Rettig, E. Affeldt, R.F. Singer, Effect of B, Zr, and C on Hot Tearing of a Directionally Solidified Nickel-Based Superalloy, Metallurgical and Materials Transactions A 47 (2016) 2914–2926. https://doi.org/10.1007/s11661-016-3416-8.
[48] J. Zhang, R.F. Singer, Effect of Zr and B on castability of Ni-based superalloy IN792, Metallurgical and Materials Transactions A 35 (2004) 1337–1342. https://doi.org/10.1007/s11661-004-0308-0.
[49] P. Kontis, H.A.M. Yusof, S. Pedrazzini, M. Danaie, K.L. Moore, P.A.J. Bagot, M.P. Moody, C.R.M. Grovenor, R.C. Reed, On the effect of boron on grain boundary character in a new polycrystalline superalloy, Acta Mater 103 (2016) 688–699. https://doi.org/10.1016/j.actamat.2015.10.006.
[50] S. Nunez, M. Prager, E.G. Thompson, Practical solutions to strain-age cracking of Rene 41, Weld. J 47 (1968) 299–313.
[51] M.B. Henderson, D. Arrell, R. Larsson, M. Heobel, G. Marchant, Nickel based superalloy welding practices for industrial gas turbine applications, Science and Technology of Welding and Joining 9 (2004) 13–21. https://doi.org/10.1179/136217104225017099.
[52] M. Morinaga, N. Yukawa, H. Adachi, H. Ezaki, New Phacomp and its Applications to Alloy Design, in: The Minerals, Metals and Materials Society, 2012: pp. 523–532. https://doi.org/10.7449/1984/superalloys_1984_523_532.
[53] N. Yukawa, M. Morinaga, Y. Murata, H. Ezaki, S. Inoue, High performance single crystal superalloys developed by the d-electrons concept, in: Superalloys 1988 (Sixth International Symposium), TMS, 1988: pp. 225–234. https://doi.org/10.7449/1988/Superalloys_1988_225_234.
[54] K. Matsugi, Y. Murata, M. Morinaga, N. Yukawa, Realistic advancement for nickel-based single crystal superalloys by the d-electrons concept, in: Superalloys 1992 (Seventh International Symposium), TMS, 1992: pp. 307–316. https://doi.org/10.7449/1992/Superalloys_1992_307_316.
[55] R.C. Reed, T. Tao, N. Warnken, Alloys-By-Design: Application to nickel-based single crystal superalloys, Acta Mater 57 (2009) 5898–5913. https://doi.org/10.1016/j.actamat.2009.08.018.
[56] Hull FC, Estimating alloy densities, Metal Progress 96 (1969) 139–140.
[57] S. Kou, A simple index for predicting the susceptibility to solidification cracking, Weld J 94 (2015) 374s–388s.
[58] J. Liu, S. Kou, Susceptibility of ternary aluminum alloys to cracking during solidification, Acta Mater 125 (2017) 513–523. https://doi.org/10.1016/j.actamat.2016.12.028.

[59] C. Xia, S. Kou, Evaluating susceptibility of Ni-base alloys to solidification cracking by transverse-motion weldability test, Science and Technology of Welding and Joining 25 (2020) 690–697. https://doi.org/10.1080/13621718.2020.1802897.
[60] S. Tao, R. Gao, H. Peng, H. Guo, B. Chen, High-reliability repair of single-crystal Ni-base superalloy by selective electron beam melting, Mater Des 224 (2022) 111421. https://doi.org/10.1016/j.matdes.2022.111421.
[61] S. Sharma, V. Kumar, A Comprehensive Review on Multi-objective Optimization Techniques: Past, Present and Future, Archives of Computational Methods in Engineering 29 (2022) 5605–5633. https://doi.org/10.1007/s11831-022-09778-9.
[62] S. Sanchez, D. Rengasamy, C.J. Hyde, G.P. Figueredo, B. Rothwell, Machine learning to determine the main factors affecting creep rates in laser powder bed fusion, J Intell Manuf 32 (2021) 2353–2373. https://doi.org/10.1007/s10845-021-01785-0.
[63] S.K. Dewangan, A. Sharma, H. Lee, V. Kumar, B. Ahn, Prediction of nanoindentation creep behavior of tungsten-containing high entropy alloys using artificial neural network trained with Levenberg–Marquardt algorithm, J Alloys Compd 958 (2023) 170359. https://doi.org/10.1016/j.jallcom.2023.170359.
[64] F. Yang, W. Zhao, Y. Ru, Y. Pei, S. Li, S. Gong, H. Xu, Deep learning accelerates the development of Ni-based single crystal superalloys: A physical-constrained neural network for creep rupture life prediction, Mater Des 232 (2023) 112174. https://doi.org/10.1016/j.matdes.2023.112174.
[65] J. Chen, J. Chen, Q. Wang, Y. Wu, Q. Li, C. Xiao, S. Li, Y. Wang, X. Hui, Enhanced creep resistance induced by minor Ti additions to a second generation nickel-based single crystal superalloy, Acta Mater 232 (2022) 117938. https://doi.org/10.1016/j.actamat.2022.117938.
[66] V. Kalyanasundaram, A. De Luca, R. Wróbel, J. Tang, S.R. Holdsworth, C. Leinenbach, E. Hosseini, Tensile and creep-rupture response of additively manufactured nickel-based superalloy CM247LC, Additive Manufacturing Letters 5 (2023) 100119. https://doi.org/10.1016/j.addlet.2022.100119.
[67] M.T. Ribeiro, S. Singh, C. Guestrin, "Why Should I Trust You?" Explaining the Predictions of Any Classifier, in: Proceedings of the 22nd ACM SIGKDD International Conference on Knowledge Discovery and Data Mining, ACM, New York, NY, USA, 2016: pp. 1135–1144. https://doi.org/10.1145/2939672.2939778.
[68] C.H. Zenk, N. Volz, C. Zenk, P.J. Felfer, S. Neumeier, Impact of the Co/Ni-Ratio on Microstructure, Thermophysical Properties and Creep Performance of Multi-Component γ′-Strengthened Superalloys, Crystals (Basel) 10 (2020) 1058. https://doi.org/10.3390/cryst10111058.
[69] L. Zhang, Z. Huang, L. Jiang, J. Luan, Z. Jiao, C.T. Liu, Effect of Mo:W ratio on segregation behavior and creep strength of nickel-based single crystal superalloys, Materials Science and Engineering: A 744 (2019) 481–489. https://doi.org/10.1016/j.msea.2018.12.043.
[70] X. Wu, S.K. Makineni, C.H. Liebscher, G. Dehm, J. Rezaei Mianroodi, P. Shanthraj, B. Svendsen, D. Bürger, G. Eggeler, D. Raabe, B. Gault, Unveiling the Re effect in Ni-based single crystal superalloys, Nat Commun 11 (2020) 389. https://doi.org/10.1038/s41467-019-14062-9.
[71] R. Su, D. Hao, P. He, D. Wu, Q. Wang, H. Dong, H. Ma, Effect of Co on creep and stress rupture properties of nickel-based superalloys – A review, J Alloys

Compd 967 (2023) 171744. https://doi.org/10.1016/j.jallcom.2023.171744.
[72] B. Chen, P.E.J. Flewitt, A.C.F. Cocks, D.J. Smith, A review of the changes of internal state related to high temperature creep of polycrystalline metals and alloys, International Materials Reviews 60 (2015) 1–29. https://doi.org/10.1179/1743280414Y.0000000041.
[73] C.M.F. Rae, R.C. Reed, Primary creep in single crystal superalloys: Origins, mechanisms and effects, Acta Mater 55 (2007) 1067–1081. https://doi.org/10.1016/j.actamat.2006.09.026.
[74] P. Caron, T. Khan, P. Veyssière, On precipitate shearing by superlattice stacking faults in superalloys, Philosophical Magazine A 57 (1988) 859–875. https://doi.org/10.1080/01418618808204522.
[75] P.L. Taylor, G. Conduit, Machine learning superalloy microchemistry and creep strength from physical descriptors, Comput Mater Sci 227 (2023) 112265. https://doi.org/10.1016/j.commatsci.2023.112265.
[76] J. Adler, I. Parmryd, Quantifying colocalization by correlation: The Pearson correlation coefficient is superior to the Mander's overlap coefficient, Cytometry Part A 77A (2010) 733–742. https://doi.org/10.1002/cyto.a.20896.
[77] J.B. Kinney, G.S. Atwal, Equitability, mutual information, and the maximal information coefficient, Proceedings of the National Academy of Sciences 111 (2014) 3354–3359. https://doi.org/10.1073/pnas.1309933111.
[78] D. Clemens, J. Galante, W. Rostoker, The influence of grain size on the fatigue behavior of annealed 316 LVM stainless steel, J Biomed Mater Res 13 (1979) 437–441. https://doi.org/10.1002/jbm.820130308.
[79] S.L. Mannan, P. Rodriguez, THE INFLUENCE OF GRAIN SIZE ON CREEP RUPTURE PROPERTIES OF TYPE 316 STAINLESS STEEL, in: Fracture 84, Elsevier, 1984: pp. 2303–2309. https://doi.org/10.1016/B978-1-4832-8440-8.50235-0.
[80] T. Ning, T. Sugui, Y. Huajin, S. Delong, Z. Shunke, Z. Guoqi, Deformation mechanisms and analysis of a single crystal nickel-based superalloy during tensile at room temperature, Materials Science and Engineering: A 744 (2019) 154–162. https://doi.org/10.1016/j.msea.2018.11.139.
[81] Y.K. Kim, D. Kim, H.K. Kim, C.S. Oh, B.J. Lee, An intermediate temperature creep model for Ni-based superalloys, Int J Plast 79 (2016) 153–175. https://doi.org/10.1016/j.ijplas.2015.12.008.
[82] S. Liu, A.P. Stebner, B.B. Kappes, X. Zhang, Machine learning for knowledge transfer across multiple metals additive manufacturing printers, Addit Manuf 39 (2021) 101877. https://doi.org/10.1016/j.addma.2021.101877.